HEALTH AND MEDICINE

Molecular phenotyping and image-guided surgical treatment of melanoma using spectrally distinct ultrasmall core-shell silica nanoparticles

Feng Chen[1]*, Brian Madajewski[1]*, Kai Ma[2]*, Daniella Karassawa Zanoni[3], Hilda Stambuk[1], Melik Z. Turker[2], Sébastien Monette[4], Li Zhang[1], Barney Yoo[1], Peiming Chen[1], Richard J. C. Meester[5], Sander de Jonge[5], Pablo Montero[3], Evan Phillips[1†], Thomas P. Quinn[6,7], Mithat Gönen[8], Sonia Sequeira[9], Elisa de Stanchina[10], Pat Zanzonico[11], Ulrich Wiesner[2‡], Snehal G. Patel[3‡], Michelle S. Bradbury[1,12‡]

Accurate detection and quantification of metastases in regional lymph nodes remain a vital prognostic predictor for cancer staging and clinical outcomes. As intratumoral heterogeneity poses a major hurdle to effective treatment planning, more reliable image-guided, cancer-targeted optical multiplexing tools are critically needed in the operative suite. For sentinel lymph node mapping indications, accurately interrogating distinct molecular signatures on cancer cells in vivo with differential levels of sensitivity and specificity remains largely unexplored. To address these challenges and demonstrate sensitivity to detecting micrometastases, we developed batches of spectrally distinct 6-nm near-infrared fluorescent core-shell silica nanoparticles, each batch surface-functionalized with different melanoma targeting ligands. Along with PET imaging, particles accurately detected and molecularly phenotyped cancerous nodes in a spontaneous melanoma miniswine model using image-guided multiplexing tools. Information afforded from these tools offers the potential to not only improve the accuracy of targeted disease removal and patient safety, but to transform surgical decision-making for oncological patients.

INTRODUCTION

Sentinel lymph node (SLN) biopsy remains the cornerstone of surgical care for treating and staging regional nodal metastases in patients with melanoma alongside other adjuvant therapies, including immunotherapy (1). Detection of metastases in regional nodes remains a vital prognostic factor, and their reliable identification and quantification have important implications for disease staging, prognosis, and clinical outcomes (2, 3). As knowledge of cancer complexity has grown, along with the challenge of elucidating an array of critical cancer targets at the cellular and molecular levels, the need to transition from the traditional single-biomarker approach to one that uses multiple biomarkers (3, 4) as part of a multiplexed detection strategy is paramount. In addition, multiple cancer biomarkers, known to be heterogeneously expressed within and across many solid tumor types, have fueled the use of spectrally distinct fluorescence imaging technologies for simultaneously visualizing a multiplexed panel of such markers, as well as for accurately assessing their distribution in situ and ex vivo. The operating surgeon should be able to precisely interrogate and molecularly phenotype more than one disease biomarker expressed by these heterogeneous cancers in real time with high sensitivity, specificity, and resolution for successful treatment planning and better outcomes.

At present, however, there is a paucity of cancer-targeted and fluorescence-based multiplexed detection tools for precision-based intraoperative procedures, in particular detection strategies that offer improved accuracy in the molecular screening and characterization of multiple cancer targets (5) in a single setting, including those identifying micrometastatic and extranodal disease. In patients with melanoma, for instance, standard-of-care agents for SLN biopsy have historically relied on the local injection of nonspecific radiopharmaceuticals, such as ^{99m}Tc-sulfur colloid (~10 to 100 nm) or Lymphoseek (^{99m}Tc-tilmanocept, ~7 nm), that typically accumulate in macrophages, and/or blue dye before detecting radioactivity in SLN(s). The surgeon needs to be able to reliably identify and discriminate radioactive SLN(s) from adjacent tissues, as well as detect small nodes (i.e., <4 mm), which can often be missed in the head and neck region given limitations of these technologies and/or anatomic complexity.

To overcome the foregoing limitations associated with conventional radiotracer approaches, traditional near-infrared (NIR) organic dyes (e.g., Cy7) have frequently been used to visualize the tumor-draining lymphatics (6–8). However, the following well-known shortcomings (9) have limited their use: reduced lesion conspicuity with extravasation into surrounding tissues, lack of specificity, poor photophysical features (i.e., brightness) that reduce sensitivity and depth penetration, and broad emission spectra that result in destructive interference, precluding concurrent imaging of multiple dyes (i.e., multiplexing) (4, 6, 10). Although the NIR dye indocyanine

green (emission peak, ~830 nm) is approved for specific indications, it is essentially confined to interrogating superficial nodes at high concentrations (µM), as shown previously in patients with melanoma (11). Although alternative optical imaging probes are available for preclinical SLN mapping (12), including antibody-conjugated fluorophores (13, 14) and nanoparticles (15–18), applications have generally been limited to ex vivo (19) or "black box" small-animal imaging evaluations, the latter not scalable to large-animal models or humans. In the former case, the majority of agents tested are largely nontargeted and/or not optimal for clinical translation because of their large size, prolonged clearance, attendant higher background signal, and/or unresolved toxicity issues (20). Moreover, targeted optical imaging probes that can assay cancer targets while serving as imaging biomarkers are generally lacking.

Image-guided large animal–to–human translational studies are scarce given the paucity of models for surgical applications that recapitulate human disease, the need for a multichannel fluorescence camera system that can concurrently acquire spectrally distinct signals, as well as the high cost of such studies. Further, although targeted molecular imaging technologies offer the potential to create a paradigm shift in perioperative patient care by combining the high-sensitivity, three-dimensional, and quantitative capabilities of preoperative positron emission tomography (PET) with the very high spatial (60 µm or better) and temporal resolution of intraoperative fluorescence camera systems, such a next-generation strategy continues to face substantial translational hurdles. To the best of our knowledge, no such comprehensive larger-animal studies have yet been performed that use such an advanced probe-device imaging strategy.

For image-guided SLN detection and treatment, we are able to build on prior and ongoing studies: (i) a successful phase 1, first-in-human clinical trial (NCT01266096) in patients with metastatic melanoma using a first-generation ultrasmall (6 to 7 nm) fluorescent and integrin-targeting core-shell silica nanoparticle tracer (C dots) covalently encapsulating Cy5 dye (i.e., ^{124}I-cRGDY-PEG-Cy5-C dots) (21); (ii) preclinical studies demonstrating specific tumor detection in well-established melanoma models using next-generation "target-or-clear" Cornell prime dots synthesized in water (C′ dots), specifically cyclic arginine-glycine-aspartic acid-tyrosine (cRGDY)– and α-melanocyte-stimulating hormone (αMSH)–conjugated C′ dots (22, 23); and (iii) an active clinical trial in patients with head and neck melanoma using cRGDY-Cy5.5-PEG-C′ dots (NCT02106598, fig. S1) demonstrating the clinical translatability of our approach. Herein, we propose a preclinical SLN biopsy protocol that is based on preoperative PET and an optically driven intraoperative multiplexing imaging strategy adaptable to larger-animal models and patients.

To that end, we developed two renally clearable, cancer-targeted, and spectrally distinct ultrasmall fluorescent core-shell silica nanoparticles (C′ dots) and combined them with a handheld fluorescence camera system as part of an SLN biopsy procedure to improve identification, molecular phenotyping, and accurate delineation of cancerous nodes in a well-established spontaneous melanoma miniswine model. Spectrally distinct C′ dots, encapsulating NIR dye Cy5.5 or CW800, were surface functionalized with melanoma-targeting peptide αMSH or cRGDY, respectively. These probes address challenges associated with intratumoral heterogeneity of biomarker expression in patients with melanoma, particularly at different pathological stages. They also enhance sensitivity and specificity for improved detection of micrometastases, combining the superior photophysical properties of spectrally distinct, targeted C′ dots relative to free dyes with a

very high sensitivity camera system adapted for surgical assessment of biomarkers. These newer-generation NIR optical imaging tools can dynamically screen multiple cancer markers in a single setting and enable rapid and selective concurrent visualization of multiple molecular targets on tumor cell surfaces at much lower levels of target expression. We believe that this approach will serve as a transformative step to ultimately improve surgical staging and treatment and overall management of melanoma.

RESULTS

Study design

We assessed the feasibility of using a fluorescence-based multiplexing strategy for intraoperative molecular phenotyping and for guiding in vivo identification and resection of metastatic lymph nodes in a well-characterized spontaneous melanoma miniswine model (24). Preoperative PET/CT (computerized tomography) findings were used to initially identify and mark the skin overlying PET-avid SLNs before surgical treatment of these nodes. Spectrally distinct particle probes and a multichannel fluorescence camera system (Quest Spectrum, Quest Medical Imaging) were then used intraoperatively for optical imaging guidance. A schematic of this dual-modality, particle-based imaging paradigm with histologic correlation is shown in Fig. 1.

Ultrasmall (hydrodynamic diameters below 10 nm) fluorescent and poly(ethylene glycol) (PEG)–coated core-shell silica nanoparticles (C′ dots), each incorporating a distinct deep/NIR organic dye and surface adapted with different peptides targeting either melanocortin-1 receptor, or MC1R (i.e., αMSH-PEG-Cy5.5-C′ dots), or α_v integrins (i.e., cRGDY-PEG-CW800-C′ dots) on malignant melanoma cells, were synthesized using a modified water-based synthetic protocol (25, 26). The cRGDY-PEG-CW800-C′ dots were also radiolabeled with positron-emitting iodine-124 (^{124}I; $t_{1/2}$ = 4.2 days) (21, 27) before intradermal injection (Fig. 1, steps 1 and 2). A preliminary CT scan was first acquired to evaluate the presence of abnormal (i.e., enlarged) lymph nodes in the region of the primary cutaneous melanomatous lesion (labeled with a radio-opaque skin tag). High-resolution PET/CT imaging was then acquired as a presurgical planning step, in addition to obtaining a dedicated whole-body PET/CT scan, to identify the tumor-draining lymphatics and any PET tracer–avid SLN(s) (Fig. 1, step 3). Following CT confirmation of these findings, sites on the skin overlying any suspicious lymph nodes were marked to guide surgical assessments (Fig. 1, step 4). Animals were then transported to the surgical suite, where image-guided multiplexed detection of SLNs was performed following local, intradermal injections of nonradioactive ("cold") cRGDY-PEG-CW800-C′ dots and αMSH-PEG-Cy5.5-C′ dots. The fluorescence camera system was used to simultaneously track optical signals from both particle probes to the draining SLN(s), in addition to localizing any higher-tier (i.e., more distal) nodes or other suspicious-appearing lymphatic tissues (Fig. 1, step 5). Nodes were surgically resected, then subjected to additional ex vivo imaging, and sent for histopathological analyses [i.e., hematoxylin and eosin (H&E), staining for melanoma markers, and tumor burden] (Fig. 1, steps 6 and 7). Correlation analyses between the nodal PET and optical imaging signals and the nodal tumor burden were performed (Fig. 1, step 8).

Development of spectrally distinct ultrasmall C′ dots

Two targeted C′ dot batches, each encapsulating a different NIR fluorescent dye and surface functionalized with a different targeting
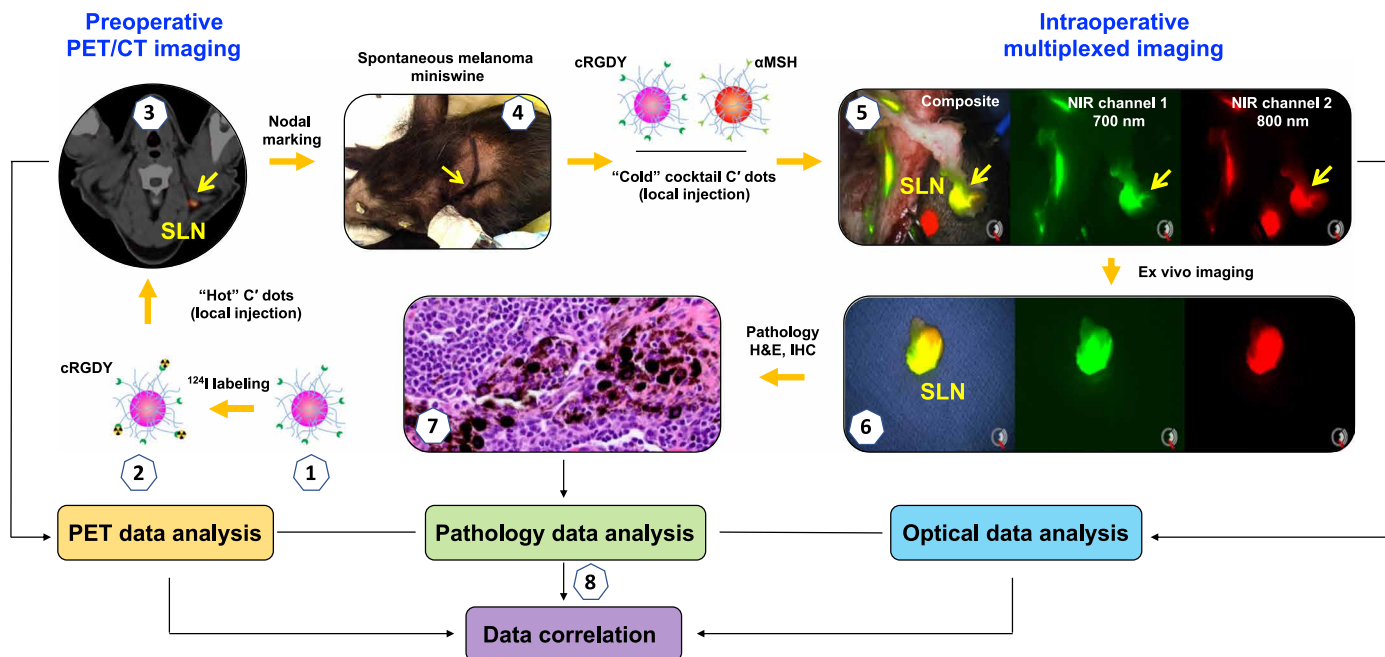
Fig. 1. A schematic illustration of the study design. Ultrasmall fluorescent core-shell silica nanoparticles, cRGDY-PEG-CW800-C′ dots (1), were first labeled with iodine-124 (^{124}I, $t_{1/2}$ = 4.2 days) to form "hot" (or radioactive) ^{124}I-cRGDY-PEG-CW800-C′ dots (2). A spontaneous melanoma miniswine was then peritumorally injected with (2) for detecting the metastatic disease based on whole-body PET/CT imaging (3). The lesion and the site of the SLN were confirmed and marked intraoperatively by a radiologist within the exposed surgical bed (4). Subsequently, serial injections of cold (or nonradioactive) αMSH-PEG-Cy5.5-C′ dots and cRGDY-PEG-CW800-C′ dots were performed peritumorally, followed by real-time multiplexed optical imaging using the Quest Spectrum imaging system (5) and resection of the nodes. Resected nodes then underwent ex vivo imaging (6) before histopathologic examination (7). Last, correlation analysis of the data derived from PET, optical, and pathological investigations was then performed (8). IHC, immunohistochemistry. (Photo credit: Feng Chen and Michelle S. Bradbury, Memorial Sloan Kettering Cancer Center)

ligand, were developed and characterized for optical imaging applications. The optical profiles of these spectrally distinct C′ dots were well aligned with the laser excitation wavelengths (i.e., ~680 and ~790 nm for Cy5.5 and CW800, respectively) on the Quest Spectrum multichannel fluorescence camera system for maximizing particle detection sensitivity. Figure 2A shows a schematic of the particle synthesis steps (25, 26) used to produce αMSH-PEG-Cy5.5-C′ dots (Fig. 2B, left) and cRGDY-PEG-CW800-C′ dots (Fig. 2B, right) via a synthesis approach with water as solvent. Specifically, Cy5.5 dye [excitation (Ex), 675 nm; emission (Em), 693 nm] was selected for the first NIR window (Fig. 2C) (25). A slight red-shift in absorbance and emission spectra was observed for the Cy5.5-encapsulating C′ dots (i.e., PEG-Cy5.5-C′ dots) when compared with the free Cy5.5 dye (fig. S2, B and C). From the combined fluorescence correlation spectroscopy (FCS; fig. S2A) and optical spectroscopy results (28), each PEG-Cy5.5-C′ dot contained, on average, about 1.7 Cy5.5 dye molecules with a 1.5-fold–per–dye quantum enhancement (fig. S2C), leading to a 2.6-fold enhanced fluorescence for the dot as compared with that of free Cy5.5 dye (table S1). The number of dyes per particle and fluorescence enhancements essentially stayed the same when moving to targeted dots by conjugating around eight αMSH peptides on the particle (Fig. 2E). Figure S3A shows a representative transmission electron microscopy (TEM) image of αMSH-PEG-Cy5.5-C′ dots demonstrating the high size homogeneity of C′ dots (29). FCS measurements further revealed an average hydrodynamic diameter of 6.4 nm (fig. S3B). The absorption and emission profiles of the αMSH-

PEG-Cy5.5-C′ dots are concordant with the first NIR detection window (690 to 740 nm) of the Quest Spectrum imaging system (fig. 2C).

For 800-nm dye-encapsulating particles, three NIR-dye candidates were tested, including DY782 (Ex, 768 nm; Em, 792 nm), DY800 (Ex, 771 nm; Em, 790 nm), and CW800 (Ex, 775 nm; Em, 792 nm), thereby creating C′ dots matching the second NIR window of the imaging system. Red-shifts in absorption (fig. S2, E, H, and K) and emission spectra, the latter revealing substantial fluorescence quantum enhancements over free dye (fig. S2, F, I, and L), were observed after encapsulating all three dyes into the C′ dot silica matrix. The per-dye quantum enhancement for PEG-DY782-C′ dots relative to free DY782 dye was found to be more than an order of magnitude (fig. S2F and table S1), likely because of both the enhanced rigidity of the silica matrix surrounding the encapsulated dyes and the specific physico-chemical nature of the dye molecules (30–33). FCS results suggested that all three C′ dot candidates had an average hydrodynamic diameter of around 5 to 6 nm, with the number of dyes per particle ranging from 1.7 to 3.0 (fig. S2, D, G, and J, and table S1). The combination of enhanced per-dye brightness and encapsulation of more than one dye molecule per particle yielded a substantially enhanced C′ dot brightness as compared with free dye for all three samples. The CW800-encapsulating probes, referred to as PEG-CW800-C′ dots, exhibited an emission maximum well shifted away from the 795-nm excitation light source (fig. S2L) and showed a particle brightness of almost an order of magnitude higher when compared with free CW800 dye (table S1) in the second NIR wavelength window of the camera system.
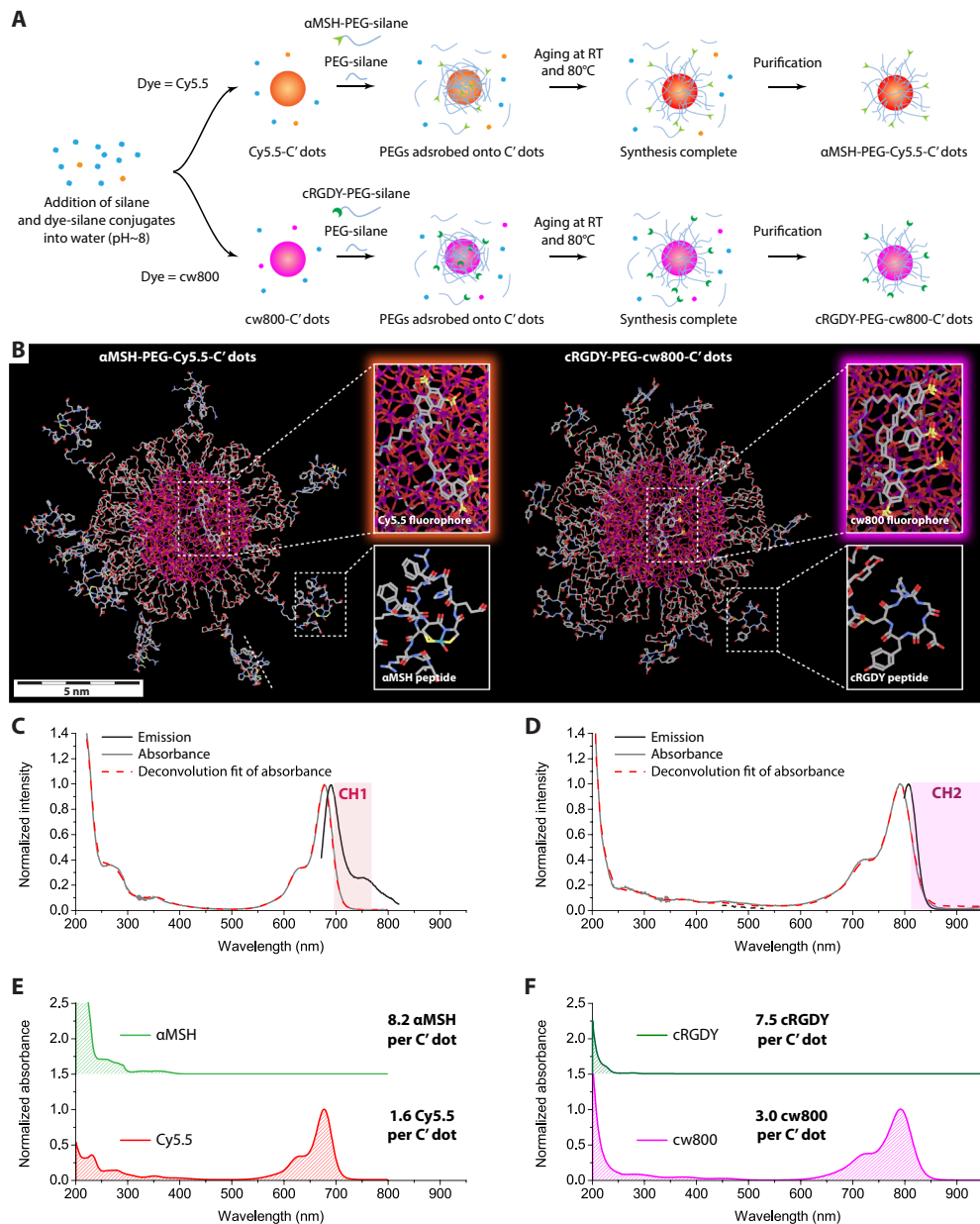
Fig. 2. Synthesis and characterization of ultrasmall tumor-targeted and spectrally distinct C' dots. (**A**) Schematic illustration of the water-based synthetic steps used to develop the two C' dots, each incorporating a distinct near-IR dye and a specific type of tumor-targeting peptide. RT, room temperature. (**B**) Three-dimensional renderings of αMSH-PEG-Cy5.5-C'-dots (left) and cRGDY-PEG-CW800-C'-dots (right). Silicon, oxygen, carbon, nitrogen, sulfur, and rhenium are colored purple, red, gray, blue, yellow, and green, respectively. Hydrogen atoms are not shown. (**C** and **D**) Emission and absorbance spectra with deconvolution fits (absorbance only) for αMSH-PEG-Cy5.5-C'-dots (C) and cRGDY-PEG-CW800-C'-dots (D). For comparison, the spectral windows of the two near-IR channels of the Quest imaging system are highlighted in these spectra. (**E** and **F**) Deconvoluted absorbance spectra for αMSH-PEG-Cy5.5-C'-dots (E) and cRGDY-PEG-CW800-C'-dots (F) allowing quantification of the per-particle αMSH ligands and Cy5.5 dyes as well as cRGDY ligands and CW800 dyes, respectively. (Photo credit: Kai Ma and Ulrich Wiesner, Cornell University)

These dots were therefore selected as the lead candidate for the multiplexing study. Figure S3D shows a TEM image of the narrowly size-dispersed cRGDY-functionalized PEG-CW800-C' dots (i.e., cRGDY-PEG-CW800-C' dots) with an average hydrodynamic diameter of 5.9 nm, 7.5 cRGDY peptides, and 3.0 CW800 dyes per particle (Fig. 2, E and F). The absorption/emission profiles of final cRGDY-PEG-CW800-C' dots matched with the second NIR detection window (i.e., >800 nm) of the imaging system (Fig. 2D). Meanwhile, gel

permeation chromatography (GPC) elugrams of both final C' dot batches showed a single peak that could be well fitted by a single-component Gaussian distribution (fig. S3, C and F), confirming high purity and narrow particle size distribution of both final products.

Camera detection sensitivity and bleed-through

The major components of the Food and Drug Administration (FDA)–cleared Quest Spectrum fluorescence imaging system (Fig. 3A)

consist of a platform, a light engine, and a camera. The light engine delivers white light and illumination (i.e., excitation) light well tuned to the measured excitation wavelengths of ultrabright Cy5.5- and CW800 dye–encapsulated particles (i.e., ~700 and 800 nm, respectively), while the camera can simultaneously image three channels, corresponding to 700- and 800-nm fluorescence signals, as well as an RGB (white-light) color channel. To determine the lower limit of fluorophore detectability at these wavelengths, as well as fluorescence signal bleed-through (which reflects the ability of the system to reliably discriminate component wavelengths), a series of in vitro and in vivo measurements (conducted in 96-well plates and small-animal models, respectively) were acquired using serial dilutions of nonradioactive αMSH-PEG-Cy5.5-C′ dots and cRGDY-PEG-CW800-C′ dots—alone and in combination.

In vitro detection sensitivity measurements using spectrally distinct fluorescent particle probes as separate preparations or as a cocktail are summarized in Fig. 3 and fig. S4. For nonmultiplexed detection assays (i.e., a single type of C′ dot and single-laser excitation), the nonzero net (i.e., background subtracted) Cy5.5 emission signal of αMSH-PEG-Cy5.5-C′ dots in the 700-nm channel, as well as the CW800 emission signal of cRGDY-PEG-CW800-C′ dots in the 800-nm channel, was achieved for particle concentrations as low as ~8 nM (Fig. 3B) and ~16 nM (Fig. 3C), respectively; these represent the respective minimum detectable fluorophore concentrations. High detection sensitivity (~16 nM) was also found for a cocktail of C′ dots over a range of concentrations (0 to 1000 nM), with both 700- and 800-nm excitation lasers turned on during the multiplexing study (Fig. 3D). In all cases (Fig. 3, B to D), signal intensity was found to increase linearly with particle concentration, saturating at concentrations of about 125 nM. A maximum of ~4% signal bleed-through to the 800-nm channel was observed when αMSH-PEG-Cy5.5-C′ dots were excited with a 700-nm laser (particle concentration range, 0 to 125 nM; fig. S5), while no significant bleed-through was detected in the 700-nm channel when cRGDY-PEG-CW800-C′ dots were excited with an 800-nm laser (fig. S6). Similar results were observed when a cocktail of C′ dots was excited with both lasers (fig. S7). Together, these results underscore the feasibility of performing simultaneous fluorescence-based multiplexed detection by exploiting both the superior photophysical properties of spectrally distinct NIR dye–encapsulating particles relative to free dye and the sensitive optics of the camera system to achieve high detection sensitivity with low signal interference (i.e., cross-talk) between the Cy5.5 and CW800 fluorophores.

For in vivo sensitivity studies, nu/nu mice were injected subcutaneously with a cocktail of C′ dots that ranged in concentration from 0.15 to 15 μM (Fig. 3E1), a factor of 10- to 1000-fold higher than that used to establish in vitro detection thresholds (vide supra). Using the 700-nm laser of the camera, excitation of αMSH-PEG-Cy5.5-C′ dots (in the 700-nm channel) resulted in fluorescence emission signals that could be sensitively detected down to a concentration as low as 0.15 μM (Fig. 3E2), and with virtually no signal bleed-through (~1%; table S2) into the 800-nm channel. Increased but still low bleed-through (i.e., 7 to 17%; table S2) and emission signal saturation were observed, however, when using particle concentrations of 1.5 μM or higher (Fig. 3E, 2 and 3, inset). As expected, an increased emission signal in the 800-nm channel was detected when the same mouse was excited with the 800-nm laser alone (Fig. 3E, 4 and 6). Similar to findings observed for the in vitro sensitivity evaluation, no detectable bleed-through was

detected in the 700-nm channel following excitation of cRGDY-PEG-CW800-C′ dots (Fig. 3E5).

Preoperative PET/CT and intraoperative multiplexing for SLN detection and treatment

Clinical PET is one of the most sensitive imaging modalities used in the clinic, which is not limited by tissue penetration depth, and provides quantitative readouts of tracer accumulation that may be correlated with key histological features. However, the spatial resolution on clinical PET scanners, about 5 to 6 mm, is relatively coarse. To overcome this limitation, we combined PET/CT with optical fluorescence imaging using the particle as an "all-in-one" platform to achieve orders of magnitude higher spatial resolution (i.e., <60 μm for the Quest Spectrum fluorescence imaging system), greater depth penetration, and quantitative readouts, potentially offering improvements to a paradigm of perioperative care that has traditionally relied on nonspecifically localizing, single-agent protocols.

High-resolution nodal-bed and whole-body PET/CT scans were initially acquired in Sinclair miniature swine ($n = 7$) following local injection of an ^{124}I-labeled cRGDY-PEG-CW800-C′ dot tracer intradermally and peritumorally about primary cutaneous lesions. This miniswine model, which spontaneously develops malignant melanoma metastatic to local/regional lymph nodes, is a clinically relevant model system demonstrating pathologic similarities with human melanoma (24). Table S3 and fig. S8 summarize the injection information [19 to 28 megabecquerels (MBq) injected per pig] and maximum intensity projection (MIP) PET images of ^{124}I-cRGDY-PEG-CW800-C′ dots in all seven pigs (movies S1 to S7). Intraoperative fluorescence-based multiplexing was subsequently performed on all miniswine after administering serial intradermal injections of nonradioactive cRGDY-PEG-CW800-C′ and αMSH-PEG-Cy5.5-C′ dots about the same cutaneous lesions and subsequently tracking particle flow within the tumor-draining lymphatics using the Quest Spectrum camera. For these injections, a microdosing strategy was used, whereby ~3.5 nmol of each fluorescent particle was serially administered [i.e., ~0.5 ml of a 7.5 μM solution of particles suspended in deionized (DI) water]. The entire in vivo and ex vivo multiplexing study, including the surgical treatment of SLN(s), was monitored in real time by video recording.

Image-guided surgical treatment of a representative miniswine with malignant melanoma (pig #5) is illustrated in Fig. 4. Preoperative PET/CT was used for surgical planning followed by multiplexed detection of these metastatic nodes intraoperatively before their resection. At approximately 1 hour after injection (Fig. 4A1), two PET-avid SLNs, labeled SLN #1 and SLN #2, were identified in the neck, along with the draining lymphatic channels. Increased activity was also noted in the bladder and the thyroid gland (Fig. 4A, 1 and 3) despite thyroid blocking by administration of potassium iodide solution. High-resolution axial CT and PET/CT images of the neck (Fig. 4B) were acquired at these nodal levels, with SNL #1 and SNL #2 (yellow arrows) demonstrating increased particle tracer uptake in Fig. 4B (2 and 4, respectively). Quantitative PET imaging analysis revealed a very high standard uptake value (SUV) of 73.3 and a tumor-to-muscle (T/M) ratio of 568.2 for SLN #1, which was nearly threefold that of SLN #2 (SUV = 26.5; T/M = 205.4). Before surgery, skin areas overlying the SLNs were marked, as shown in fig. S9.

Key frames selected from real-time video footage of pig #5 (movie S8) are shown in Fig. 4C. From Fig. 4C1, no obvious nodal pathology could be identified in the surgical bed under white-light conditions

(RGB color channel) to guide the SLN mapping procedure. However, with the serial injection of both particle probes and with both lasers simultaneously illuminating the nodal bed, strong NIR fluorescence signals were detected at the site of injection (white arrow, Fig. 4C2)

and within the draining tumor lymphatics. The individual 700- and 800-nm fluorescence channel data (Fig. 4C, 3 and 4, pseudocolored in green and red, respectively) for each particle probe, as well as the composite images generated from projection of these data onto the
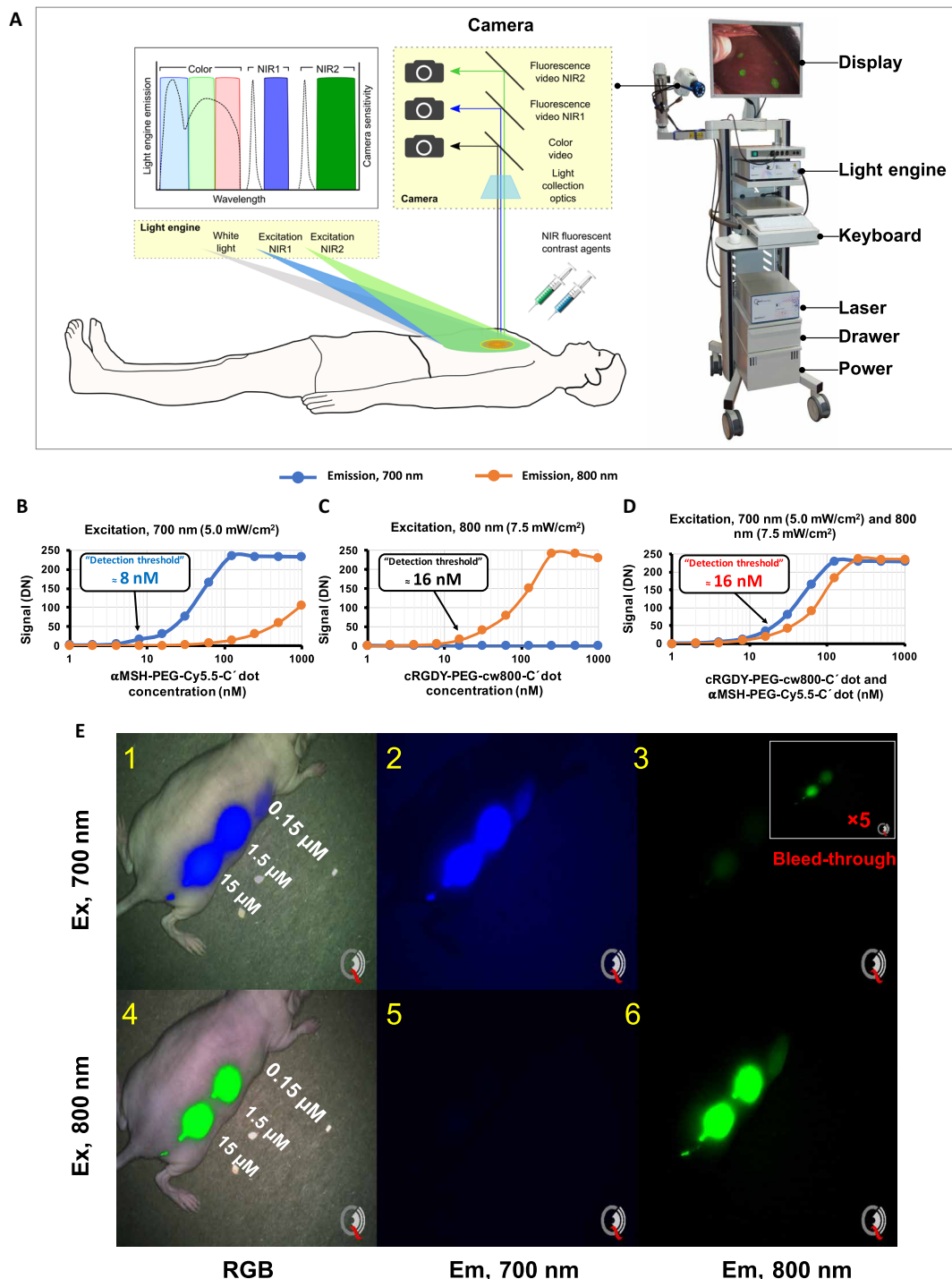
Fig. 3. Schematic and photo of the Quest Spectrum camera system and its detection sensitivity to C' dots. (**A**) Schematic of the Quest Spectrum camera system illustrating RGB (white), 700 NIR1 (blue), and 800 NIR2 (green) channels. (**B** to **D**) Optical intensity versus C' dot concentration relationship under single (B and C) or combined (D) laser excitation. (**E**) In vivo optical imaging of a mouse subcutaneously injected with mixtures of αMSH-PEG-Cy5.5-C' dots and cRGDY-PEG-CW800-C' dots at different concentrations (0.15 to 15 μM). Left: RGB channel. Middle: 700-nm emission channel (blue pseudocolor). Right: 800-nm emission channel (green pseudocolor). Right upper inset shows bleed-through of the 700-nm (blue) channel into the 800-nm (green) channel. (Photo credit: Richard J. C. Meester, Quest Medical Imaging and Feng Chen, Memorial Sloan Kettering Cancer Center)
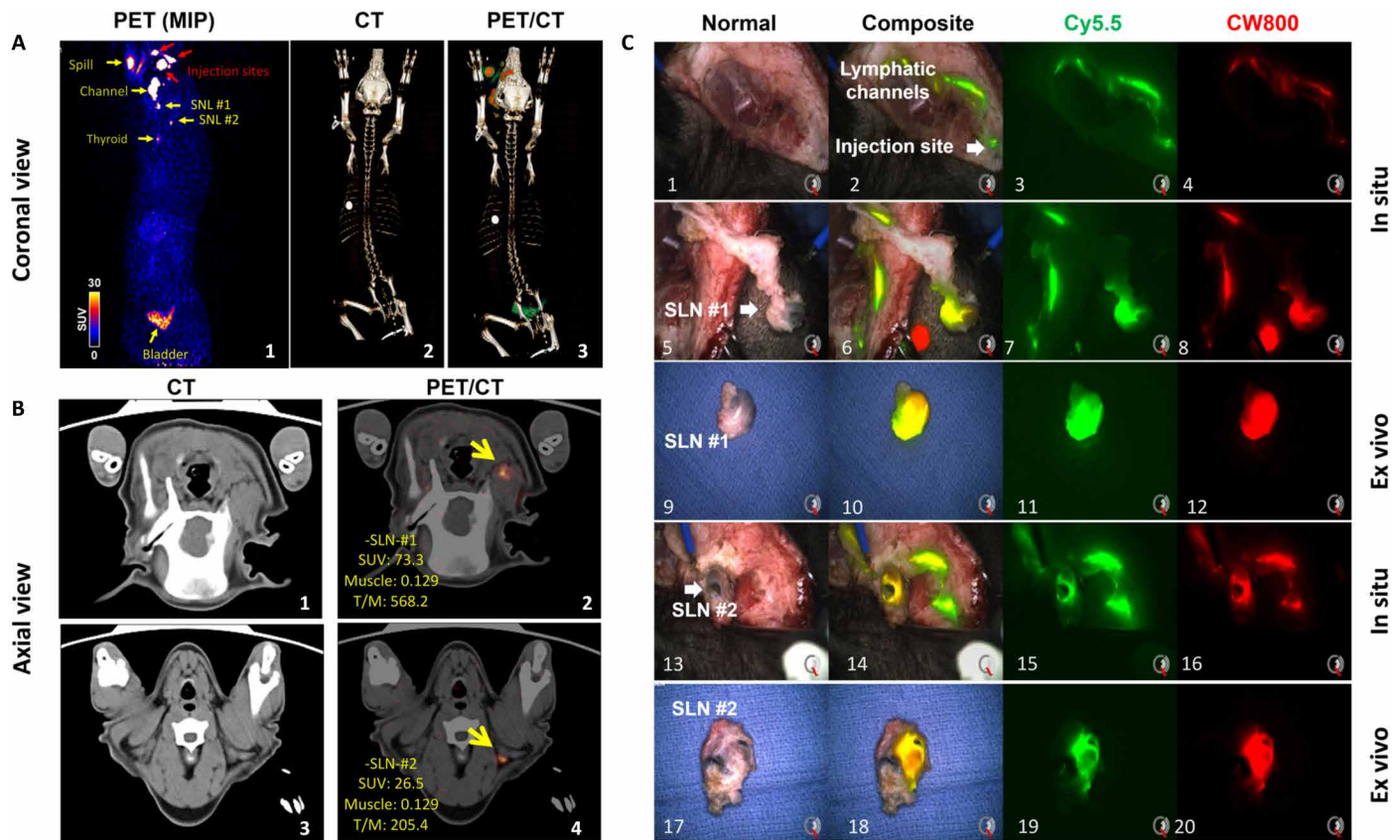
Fig. 4. Preoperative PET/CT and real-time intraoperative multiplexed optical imaging of a representative spontaneous melanoma miniswine (pig #5). (**A**) Whole-body PET/CT images (coronal view). A1: PET only (injection sites marked in red); A2: CT image; A3: PET/CT fusion image. (**B**) CT and PET/CT axial view images. SNL #1 and SNL #2 are marked with yellow arrows in B2 and B3, respectively. (**C**) Selected frames from the recorded real-time surgical video footage (movie S8). (1, 5, 9, 13, and 17) Bright-field images of surgical site, in situ SLN #1, ex vivo SLN #1, in situ SLN #2, and ex vivo SLN #2, respectively. (2, 6, 10, 14, and 18) Corresponding composite images of Cy5.5 and CW800 emission channels. The injection site (white arrow) and lymphatic channels are highlighted. (3, 7, 11, 15, and 19) Corresponding Cy5.5 emission channel images (green pseudocolor). (4, 8, 12, 16, and 20) Corresponding CW800 emission channel images (red pseudocolor). (Photo Credit: Daniella Karassawa Zanoni, Hilda Stambuk, Snehal G. Patel, and Feng Chen, Memorial Sloan Kettering Cancer Center)

RGB color channel, were used not only to better facilitate surgical resection of nodes but also for molecular phenotyping of the nodal tissue, that is, to determine the expression of the targeted cancer biomarkers (i.e., integrin α_v, MC1R). Heterogeneities in the magnitude and distribution of optical signals within the nodal tissue may reflect variations in the expression profiles of these markers and/or variability in cancer phenotype.

The two SLNs from pig #5 were carefully exposed (Fig. 4C, 5 to 8, SLN #1; Fig. 4C, 13 to 16, SLN #2) and resected on the basis of real-time multiplexed detection of spectrally distinct targeted particles. The ex vivo (Fig. 4C, 9 to 12, SLN #1, and 17 to 20, SLN #2) target-to-background ratios of SLN(s) in both NIR channels, one of our study endpoints, were estimated to be at least 200 as a result of the very high fluorescence signals detected, as well as the negligible auto-fluorescence or other background signal. The optical imaging data analysis performed is shown in fig. S10 for a representative multiplexing study. Last, the nodal bed was carefully inspected using the camera system to verify that no residual optical signal remained at the site of resection. A total of 13 nodes were resected from all seven miniswine using the same image-guided procedures (table S4).

Collectively, these data convincingly demonstrate that targeted and spectrally distinct fluorescent particle probes are capable of being multiplexed to reliably, sensitively, and concurrently detect diverse cancer biomarkers expressed by in vivo and ex vivo resected lymph nodes in a clinically relevant spontaneous melanoma miniswine model using an optimized particle-based microdosing strategy and real-time imaging guidance. High target-to-background ratios, obtained as part of our PET/CT and fluorescence-based multiplexing studies, using an integrin-targeting C′ dot PET tracer and spectrally distinct nonradioactive C′ dots, respectively, serve to provide an initial framework for next-stage clinical trial designs.

Ex vivo histological analysis

Lymph node specimens ($n = 13$; table S4) were collected for all miniswine and subjected to ex vivo histological analyses to assess for the presence of metastasis, quantify metastatic tumor burden on the basis of maximum tumor deposit diameter or the amount of melanin, and to evaluate the expression of target markers integrin α_v and microphthalmia-associated transcription factor (MiTF), a well-described downstream effector of MC1R signaling (34). Of the 13 SLNs harvested from seven miniswines, 9 were found to be metastatic, while the remaining 4 predominantly revealed melanophages, or macrophages containing a melanin pigment (Table 1). However, the possibility of coexistent melanoma cells in the latter specimens

could not be entirely excluded as only a limited number of nodal sections per node were reviewed in each case. There were no false-negative findings. Results additionally gathered by a pathologist (S.M.) demonstrated a wide range in tumor burden values, measured as maximum tumor deposit diameter, across all collected specimens (Table 1 and table S4) (35–37). It is worth noting that variations in the sizes of metastatic deposits within lymph nodes occurred not only among animals but also in different nodes excised from the same animal, thus demonstrating the heterogeneous nature of metastasis in the spontaneous melanoma miniswine. A representative set of lymph nodes resected from a single miniswine (pig #5) with varying degrees of tumor burden is depicted in Fig. 5. Large metastatic melanoma deposits (maximal tumor burden diameter, 5.7 mm; table S4) were exhibited by SLN #1 (Fig. 5, A to D), while SLN #2

Table 1. Histopathological summary of lymph nodes resected from metastatic melanoma miniswine: Molecular phenotypes, tumor burden, and metastatic disease. Summary of lymph node mapping data (n = 13 nodes) resected from seven metastatic melanoma miniswine (columns 1 and 2) including one or more of the following: (i) H&E staining to assess for the presence of malignancy, (ii) quantitation of tumor burden, and (iii) molecular phenotype by immunohistochemistry (IHC). To address cancer heterogeneity, IHC was performed to assay key molecular markers expressed by melanoma cells: integrin α_v (column 3) and MiTF (column 4), the latter induced by activation of melanocortin-1 receptor expression on the cell surface. MiTF, along with H&E staining, was used to refine our final pathological diagnoses (column 5), as it served as a specific marker to discriminate melanoma cells from melanophages (histiocytes that have phagocytozed melanin). Tumor burden (column 6) was quantified on the basis of the maximum diameter of the largest pigmented cell focus within nodes; this parameter was found to outperform other measurements of metastatic/micrometastatic tumor burden in a recent large clinical trial series (35). NP, not provided.

Miniswine #		Molecular phenotypes		Pathology	Tumor burden	
		Integrin α_v	MiTF	H&E	Max diameter (mm)	Melanin content (mm²)
#1	Right SLN	Not performed (NP)	NP	Metastatic melanoma, melanophages	2.5	63.1
	Right inguinal node	NP	NP	Metastatic melanoma, melanophages	2.0	88.4
#2	Left: SLN #1	2 to 3+, membrane (rare cells)	+ (rare cells)	Metastatic melanoma, abundant melanophages*	13.2	191.7
#3	Right: SLN #1	2 to 3+, membrane (rare cells)	+ (rare cells)	Metastatic melanoma, abundant melanophages*	8.2	147.3
	Pelvic node	2 to 3+, membrane (rare cells)	+ (rare cells)	Metastatic melanoma, abundant melanophages*	2.1	13.9
#4	Left: SLN	0+	−	Melanophages**	−	0.3
	Right: SLN	0+	−	Melanophages**	−	0
#5	Left: SLN #1	3+, membrane (rare cells)	+ (rare cells)	Metastatic melanoma, abundant melanophages*	5.7	384.5
	Left: SLN #2	3+, membrane	+	Metastatic melanoma, abundant melanophages	0.5	0.2
#6	Left: SLN #1	3+, membrane	+ (rare cells)	Metastatic melanoma, abundant melanophages*	3.7	239.9
	Left: SLN #2	0+	−	Melanophages**	−	0.1
#7	Right: SLN	2 to 3+, membrane	+	Metastatic melanoma, melanophages	1.6	0.9
	Retroperitoneal SLN	0+	−	Melanophages**	−	2.3
#2	Primary tumor	2 to 3+, membrane	+	Melanoma, with abundant melanophages***		
#3	Primary tumor	0+	+	Melanoma, with abundant melanophages***		
#4	Primary tumor	2 to 3+, membrane	+	Melanoma, with abundant melanophages***		
#5	Primary tumor	3+, membrane	+	Melanoma, with abundant melanophages***		
#6	Primary tumor	1 to 2+, membrane	+	Melanoma, with abundant melanophages***		
#7	Primary tumor	0 to 3+, membrane	−	Regressed melanoma (abundant melanophages, no melanoma cells)		

*Melanoma cells [MiTF+, integrin+] rare.   **Cannot exclude melanoma cells.   ***Most pigmented cells are melanophages.

(Fig. 5, I to L) harbored micrometastases (maximal tumor burden diameter, 0.45 mm; micrometastases defined as <2 to 3 mm) (*35*, *37*), as determined by H&E staining (Fig. 5, A and B, and I and J) and the maximum diameter of the tumor deposit. Although melanin content was also used to assess tumor burden, this method is known to be limited by the fact that tumor deposits may exhibit only partial pigmentation, in turn leading to underestimates of this parameter. Conversely, the presence of pigmented or melanin-laden macrophages, which may be difficult to discriminate from tumor cells, can also confound these analyses.

Tissue sections adjacent to the respective H&E-stained sections were additionally evaluated for the expression of target markers integrin α_v and MiTF (Fig. 5, C and D, and K and L). Unfortunately, antibodies directed toward porcine MC1R are currently not com-mercially available. To overcome this limitation, we implemented the use of MiTF as a surrogate marker for MC1R expression. Further, as MiTF is expressed by most melanomas (*38*), immunohistochemistry (IHC) for this marker was examined on all lymph nodes, in addition to H&E-stained sections, to assist in the detection of micrometastases and their differentiation from other lymph node cell populations, such as melanophages. While MiTF immunoreactivity of human macrophages by IHC has been described with some antibodies (*39*), no staining of swine macrophages was observed with the antibody used in this study. On a subset of lymph nodes, immuno-histochemical staining for the melanocyte marker HMB-45 and the macrophage marker Iba1 was also performed to confirm the presence of micrometastasis and melanophages. Results from IHC staining confirmed the presence of both integrin α_v and
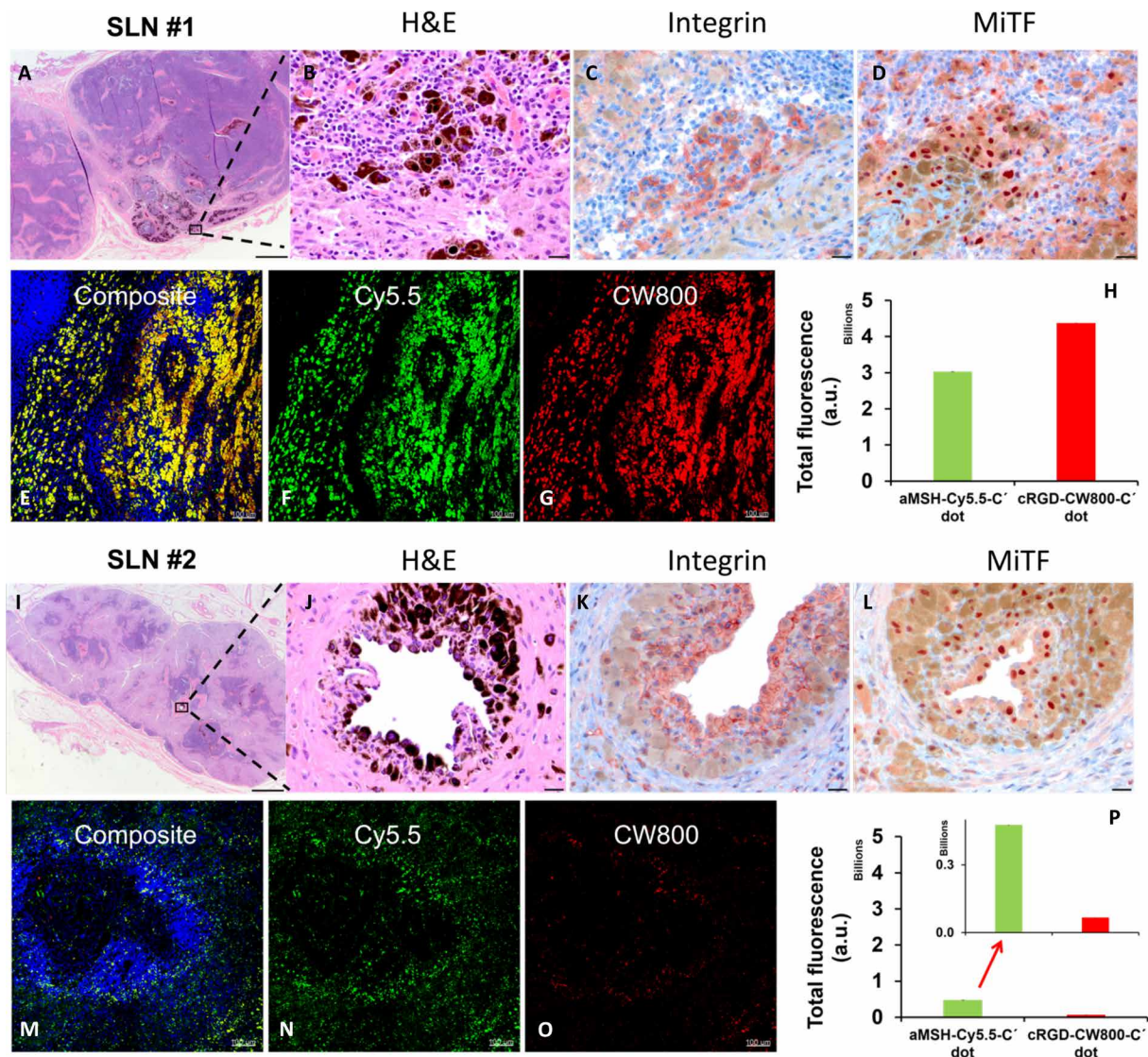
Fig. 5. Ex vivo lymph node histological investigation for pig #5. SLN #1/SLN #2: Ex vivo histological analysis illustrating (**A** and **I**) low- and (**B** and **J**) high-magnification H&E staining. (**C** and **K**) Integrin and (**D** and **L**) MiTF immunohistochemical staining. High-resolution confocal fluorescence microscopy of αMSH-PEG-Cy5.5-C′ dot and cRGDY-PEG-CW800-C′ dot merged fluorescent channels with 4′,6-diamidino-2-phenylindole (DAPI) nuclear stain (**E** and **M**). Independent display of CW800 and Cy5.5 channels (**F** and **N** and **G** and **O**, respectively). (**H** and **P**) Quantification of Cy5.5 and CW800 signals′ total fluorescence intensities as displayed in (F) and (N) and (G) and (O). Scale bars, 1 mm for (A) and (I), 20 μm for (B) to (D) and (J) to (L), and 100 μm for (E) to (G) and (M) to (O). a.u., arbitrary units. (Photo credit: Brian Madajewski and Sébastien Monette, Memorial Sloan Kettering Cancer Center)

MiTF in areas of metastatic melanoma (Fig. 5, C and D, K and L). The surrounding normal nodal tissue showed appreciably less staining for both markers, indicating their specificity for tumor. The primary tumor was histologically consistent with melanoma in all animals, except in one pig in which the tumor was composed of pigmented macrophages only, consistent with a completely regressed melanoma, a common phenomenon in this animal model (40).

Using high-resolution confocal microscopy, a clear difference in fluorescence intensities was observed between SLN #1 (high tumor burden; Fig. 5, E to G) and SLN #2 (low tumor burden; Fig. 5, M to O), respectively. Quantification of the total fluorescence across the field of view demonstrated a ~65-fold greater cRGDY-PEG-CW800-C′ dot particle intensity (Fig. 5, H and P, red bars), as well as a ~6-fold increase in αMSH-PEG-Cy5.5-C′ dot intensity (Fig. 5, H and P, green bars), when comparing the high-burden lymph node (SLN #1) to the low-burden one (SLN #2). In addition, both the CW800 and Cy5.5 signals strongly colocalized with one another (Fig. 5, E and M), indicating both integrin α_v and MC1R targets were coexpressed on metastatic melanoma deposits, a finding previously confirmed via immunohistochemical staining.

All collected nodal specimens from individual miniswine were subjected to identical analyses and demonstrated similar results (figs. S11 to S16). The combination of histopathological assays performed provided complementary information on the detailed populations present within these nodal specimens. On confocal microscopy, at least one or more focally dense distributions of increased particle signal were observed for each target. One exception to this distribution pattern was found for a small retroperitoneal SLN in pig #7 (fig. S16). When comparing the measured intensity sums of the SLN and retroperitoneal SLN, the values closely approximated one another; however, visual inspection of Cy5.5 and CW800 fluorescent signals did not appear to be equivalent. Closer inspection of these images in both channels (Cy5.5 and CW800) revealed large amounts of low-level, diffusely distributed particle fluorescence that was incorporated into the analysis, resulting in increased intensity sums across channels. These findings may reflect the fact that melanophages were predominant on the nodal tissue sections inspected. An additional possibility is that visibly different spatial distributions of target expression profiles can lead to nearly equivalent summed intensity values. These observations underscore the importance of obtaining both in-depth histopathological and spatial distribution data to deduce the best treatment management plan for a given fluorescent probe.

Together, these results demonstrated that simultaneous multi-plexed detection of diverse melanoma biomarkers in vivo could be confirmed histopathologically using spectrally distinct αMSH-PEG-Cy5.5-C′ dots and cRGDY-PEG-CW800-C′ dots. For nodal tumor deposits smaller than 2 to 3 mm in diameter (i.e., micrometastases), as well as deposits larger than 3 mm in diameter, summed optical intensities of both particle probes could be quantified as a measure of their selective accumulation and distribution at sites of disease using confocal microscopy. Optically active metastatic nodal deposits corresponded with those seen on H&E staining to assess tumor burden. Variations in the degree of tumor burden on H&E staining were accurately quantified using the maximum tumor deposit diameter. Last, pathology-proven metastatic tumor deposits demonstrated coexpression of integrin α_v and MC1R surface markers by IHC, suggesting that αMSH- and cRGDY-functionalized C′ dots are capable of specifically targeting areas of metastatic tumor deposition

in nodal specimens that express MC1R and integrin α_v target proteins, respectively.

Multimodality signal values strongly correlate with burden of lymph node metastases

Observed differences in total accumulated fluorescence across metastatic lymph nodes prompted a deeper investigation into the relationship between the deposition of melanoma and particle accumulation within diseased nodes. As observed earlier, there were not only varying levels of tumor burden across harvested samples but also nodes that demonstrated clear separation of disease from normal nodal tissue architecture (i.e., partially replaced nodes). Examination of a partially replaced lymph node is shown in Fig. 6, A to D. Using wide-field fluorescence microscopy, our analysis showed a selective accumulation of αMSH-PEG-Cy5.5-C′ dots in areas of disease (Fig. 6A1), while only low levels of accumulation were detected in adjacent normal tissue (Fig. 6A2). To provide better localization of both particle probes, high-resolution confocal microscopy was performed at selected sites of interest. In comparison to adjacent normal tissue (Fig. 6C), both αMSH-PEG-Cy5.5-C′ dots and cRGDY-PEG-CW800-C′ dots demonstrated significant accumulation in areas corresponding to melanoma deposition (Fig. 6D). Similar evaluations were carried out on representative nodes that did not have a clear delineation in metastatic localization but instead had differing degrees of diffuse disease. A representative lymph node with a low level of tumor burden showed decreased accumulation of both targeted C′ dots (Fig. 6, E to G) in relation to the node exhibiting high tumor burden (Fig. 6, H to J) by both wide-field fluorescence microscopy and higher-resolution confocal microscopy. Such a difference in C′ dot accumulation could be explained by the differential expression levels of MC1R in these tissue specimens, as demonstrated by Western blot analyses, in which the latter showed considerable variations in MiTF expression (Fig. 6K).

With strong evidence indicating a relationship between the level of metastatic disease and C′ dot accumulation, we sought to correlate the level of tumor burden with acquired PET activities and optical signal intensities. For the particle tracer (i.e., ^{124}I-cRGDY-PEG-CW800-C′ dots), we measured tumor-to-background (T/B) ratios on the basis of SUV and correlated these values with the maximum diameter of metastatic deposits (table S4 and figs. S11 to S16). Using linear regression analysis, it was determined that T/B ratios demonstrated a very strong positive correlation with measured tumor burden, with an $R^2 = 0.916$ (Fig. 6L). Similarly, plotting total fluorescence values of cRGDY-PEG-CW800-C′ dot particles gathered from all nodes (Fig. 5 and figs. S12 to S16) against their respective tumor burden values also resulted in a strong imaging-tissue correlation ($R^2 = 0.855$; Fig. 6M), indicating that particle imaging findings could predict tumor burden at nodal metastatic sites.

It is important to note that while the high-sensitivity whole-body PET/CT imaging played a key role in detecting metastatic nodes during the preoperative planning step, however, its ability to delineate heterogeneous tumor distributions and micrometastatic disease within nodes was significantly limited due to the relatively coarse spatial resolution of clinical PET (i.e., ~5 to 6 mm). By combining these PET evaluations with high-resolution optical imaging of tumor-targeted, spectrally distinct C′ dots using the Quest Spectrum fluorescence imaging system (i.e., <60 μm) and confocal microscopy, we were able to (i) reliably and accurately localize
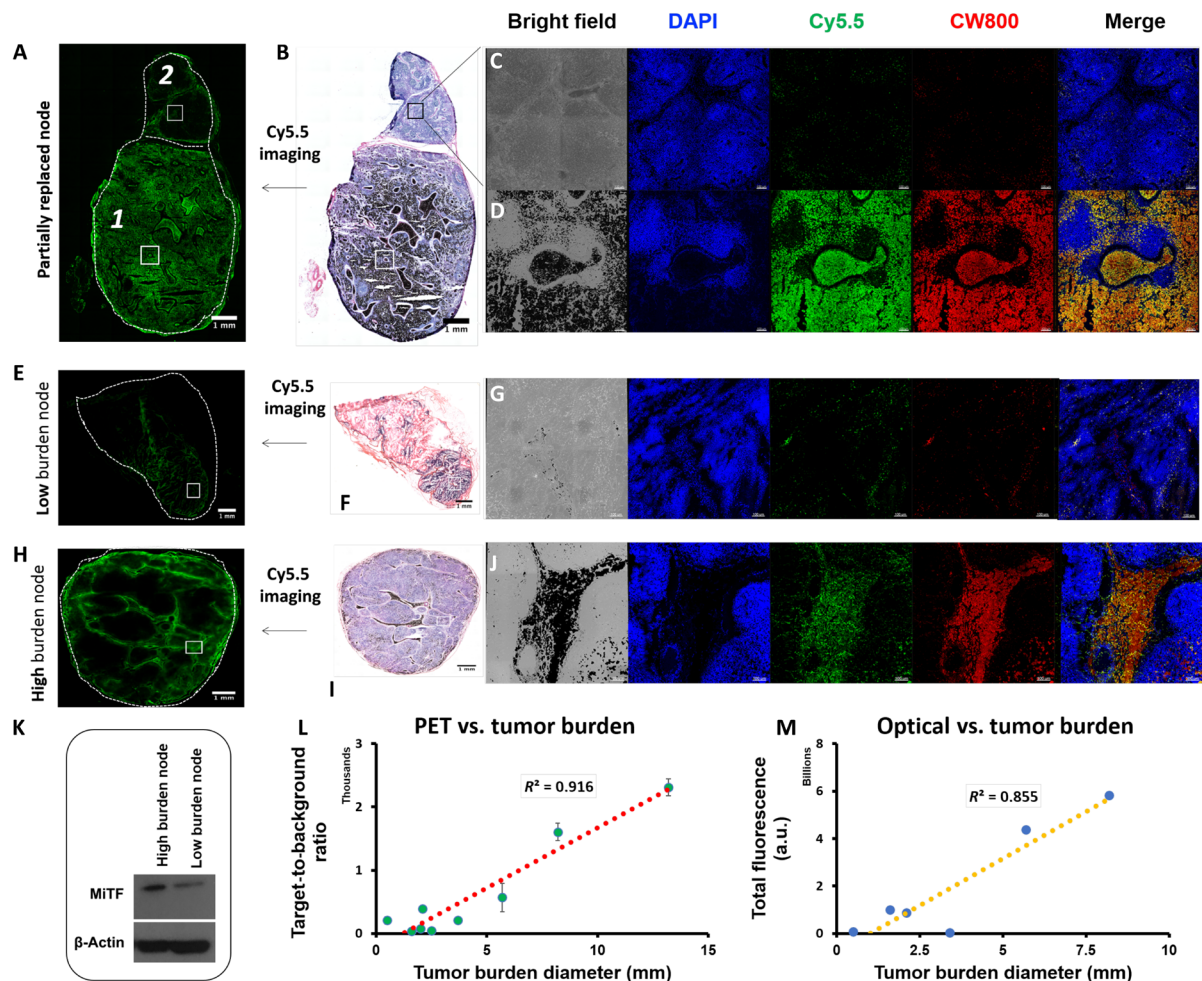
Fig. 6. Multimodal (PET/optical) signal values strongly correlate with burden of lymph node metastases. (**A**) Wide-field Cy5.5 fluorescence microscopy and bright-field (**B**) imaging of H&E-stained partially replaced lymph node. Scale bars, 1 mm. High-resolution confocal microscopy of partially replaced lymph node regions corresponding to normal (**C**) and tumor-containing areas of tissue (**D**). Scale bars, 100 μm. (**E** and **H**) Cy5.5 wide-field fluorescence microscopy of a representative low- and high–tumor burden lymph node, respectively. H&E staining of adjacent tissue sections (**F** and **I**). Scale bars, 1 mm. Confocal microscopy demonstrating decreased αMSH-PEG-Cy5.5-C′ dot and cRGDY-PEG-CW800-C′ dot signal in a low-burden lymph node (**G**) in comparison to a node with high-tumor burden (**J**). Scale bars, 100 μm. (**K**) Western blot of the high– and low–tumor burden nodes showing the variation in MiTF expression. Correlation across all lymph nodes of PET target-to-background ratios with $R^2 = 0.916$ (**L**) and total fluorescence values for accumulated cRGDY-PEG-CW800-C′ dots with $R^2 = 0.855$ (**M**) as a function of measured tumor burden. (Photo credit: Brian Madajewski and Sébastien Monette, Memorial Sloan Kettering Cancer Center)

metastatic SLNs in a large-animal miniswine model (Fig. 4) using real-time, image-guided multiplexed detection and (ii) sensitively map particle distributions, intranodal tumor heterogeneity, and micrometastatic foci on the basis of ex vivo whole-node signal detection methods (Figs. 5 and 6).

Toxicity evaluation to support a multiplexing trial design at the microdosing level

To support a future image-guided multiplexed detection strategy in patients with melanoma, dual-probe, single-dose acute toxicity testing was conducted by using subcutaneous injections of 1.2 nmol of both αMSH-PEG-Cy5.5-C′ dots and cRGDY-PEG-CW800-C′ dots in healthy and M21 xenografted mice (fig. S17). A total of 122 mice (61 male; 61 female) were divided into 24 groups and numbered as outlined in table S5.

In the mortality and morbidity evaluation (table S6), none of the animals in the nontumor, test article cRGDY-PEG-CW800-C′ dot groups, except for one, presented adverse signs in the parameters measured (body weights, clinical, hematology, clinical chemistry, and gross necropsy), suggesting that the one death was not related to the test article. A single mouse (1 of 15) was found dead on study day 8 (group 23). The cause of death could not be determined because of its deteriorated body condition. In the tumor-bearing groups, four mice died because of a large tumor burden as follows: one mouse (1 of 15) died on study day 9 (group 19), two mice died on study day 11 (group 18), and one mouse died on day 11 (group 20). Tissue analyses were not performed in these animals because of their deteriorated body conditions. It is known that tumors injected subcutaneously may cause death without notable changes in clinical signs and body weights (*41*). No other animal in any of the tumor groups

presented adverse signs in any of the parameters measured (body weights, clinical, hematology, clinical chemistry, and histopathology), suggesting that the unscheduled deaths were not related to the test article, but to the tumor burden.

By study day 11, tumor size reached the permissible limit and tumor ulceration was observed in all tumor-bearing animal groups, requiring unscheduled euthanasia pursuant to institutional guidelines. No abnormal behavior or other clinical signs were recorded. There were no findings at necropsy that were considered to be toxicologically relevant. All tumors were analyzed by H&E staining and had morphology consistent with M21 human melanoma. Non–tumor-bearing mice (groups 21 to 24) were kept under observation until the scheduled end of the study (day 15). There were no findings at necropsy considered to be toxicologically relevant. Hematology (tables S7 and S10 to S29) and clinical chemistries (tables S8, and S30 to S49) were unremarkable, and body weights (figs. S18 and S19) were similar among groups. All differences between test article–treated groups and the corresponding vehicle-treated groups were within normal reference ranges or were not biologically relevant or statistically significant. No macroscopic findings were reported at the time of gross necropsy. Histopathologic lesions that were observed with similar incidence and severity in all groups were considered naturally occurring background lesions, unrelated to the test article. There were no histopathologic lesions seen that are considered toxicologically relevant. No evidence of test article–related toxicity of any target organs (table S9) was identified on either day 2 or day 14. Figure 7 shows representative H&E-stained images of mixed-gender mice from related groups on day 14. These findings suggest that a single subcutaneous injection of 1.2 nmol of either test article was well tolerated with no indications of systemic or delayed toxicity. The no observed adverse events level (NOAEL) was not determined in this single-arm investigational new drug (IND)–enabled microdose toxicity study, although the study indicates that the NOAEL is greater than 1.2 nmol for a single subcutaneous injection of either αMSH-PEG-Cy5.5-C′ dots or cRGDY-PEG-CW800-C′ dots in mice.

DISCUSSION

SLN mapping is a recognized National Comprehensive Cancer Network standard-of-care procedure for treating several early-stage solid tumors, such as melanoma. This procedure relies on human visual cues and/or tactile information as part of a more invasive procedure without the ability to identify heterogeneously expressed molecular determinants on cancerous nodes or to define the extent of nodal disease. Current SLN practice for head and neck melanoma is plagued by serious challenges, as it is principally based on the use of nonspecific radiopharmaceutical agents, such as ^{99m}Tc-sulfur colloid, which cannot accurately locate or visualize nodes nor discriminate nodal disease from non–tumor-bearing nodes. Although ^{99m}Tc-sulfur colloid has been combined with blue dye to improve SLN detection, the technique is limited by significant differences in the hydrodynamic diameters of these agents, leading to variations in nodal retention time (42). It is critical to implement more reliable and accurate image-guided multiplexing tools to address intratumoral heterogeneity and visualize disease in real time, as they represent major impediments to effective cancer treatment and precision medicine (43). Intraoperatively, these tools can also (i) provide immediate feedback on tumor markers that alter surgical
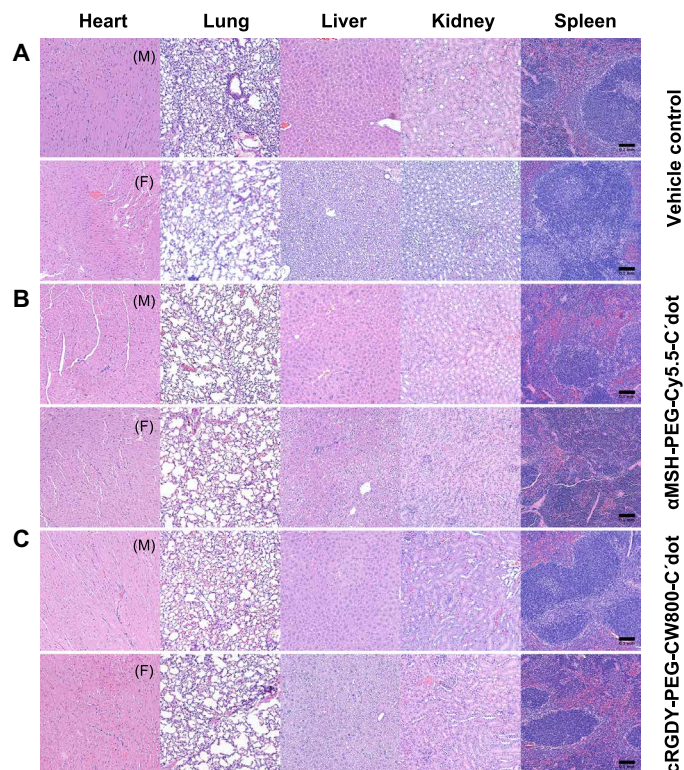
Fig. 7. Representative H&E staining images of major organs. Mice were injected with (**A**) saline vehicle (50 μl), (**B**) αMSH-PEG-Cy5.5-C′ dots (1.2 nmol), and (**C**) cRGDY-PEG-CW800-C′ dots (1.2 nmol). M, male; F, female. Scale bars, 0.1 mm. (Photo credit: Brian Madajewski, Memorial Sloan Kettering Cancer Center)

approaches and decision-making, (ii) lead to less exploratory surgery and more targeted disease removal, and (iii) thus improve safety, speed, and accuracy.

Despite decades of technological advances involving engineered nanoparticle-based probes for SLN mapping (44), there remains a paucity of optically active targeted particle probes for in vivo applications (45), hindered, in part, by translational challenges. Cornell dots (C dots) (21) are one of the few inorganic fluorescent nanoparticles that have been approved in the United States as an investigational agent for clinical SLN mapping (NCT01266096 and NCT02106598) and real-time molecular imaging guidance. These issues underscore the need for clinically translatable targeted optical imaging probes that can sensitively and specifically visualize, detect, and guide surgical treatment of cancer-bearing SLN(s). In addition, it has become increasingly important to transition to newer-generation technologies that can enable in vivo detection of multiple biomarkers as part of a multiplexed tumor detection and characterization strategy.

In this study, we showed the feasibility of using a fluorescence-based multiplexing strategy for SLN mapping by developing ultra-small (<8-nm diameter) and spectrally distinct fluorescent core-shell silica nanoparticles. The PEGylated outer layer of the particles enhanced aqueous stability and rendered the surface electrostatically neutral, thereby minimizing recognition by the immune system. It also served as a scaffold for attaching tumor-homing peptides (e.g., cRGDY and αMSH), while the NIR fluorescent dyes (e.g., Cy5.5 and CW800) were covalently encapsulated within the silica core of the particles, leading to a significant enhancement in photophysical properties (i.e., brightness) and detection sensitivity. By designing

these tumor-targeted particle probes as all-in-one multimodal imaging platforms for SLN mapping via concurrent radiolabel attachment (e.g., [124]I), preoperative PET/CT and intraoperative fluorescence-based multiplexed detection of metastatic disease could be performed in a single setting. Such an all-in-one design stands in stark contrast to the multiple probes needed in routine clinical practice for the same purpose. The implementation of these all-in-one particle probe designs is advantageous for several reasons, among others (i) both regional and systemic disease could be mapped with the same dual-modality platform for more efficient staging and treatment planning; (ii) the combination of different imaging modalities enables an expanded array of multiplexed detection capabilities for more comprehensive disease assessments both in vivo and ex vivo, which is not otherwise possible for different classes of agents; and (iii) noninvasive screening for metastatic nodes using a single intravenous injection may improve stratification of patients to appropriate treatment arms (i.e., surgical versus nonsurgical), thereby eliminating unnecessary surgical interventions.

It is important to note a few limitations of the study. First, the optical signal acquired for many of the nodes, both in vivo and ex vivo, was saturated (fig. S10), precluding precise optical quantitation of T/B ratios. In the absence of such signal saturation, T/B ratios can be used to better examine heterogeneity within individual nodes or across nodes in a given subject, or even facilitate comparisons among different subjects. However, to derive such information, a knowledge of the camera working distance, gain, and exposure time used to acquire nodal images in situ and ex vivo is needed to correct measured optical signal intensities for variations in these parameters on a case-by-case basis. Although procedures required to derive the working distance were not used as part of this study, these have now been implemented in our ongoing advanced phase 2 SLN mapping trial in patients with melanoma. Notwithstanding, from a surgical perspective, quantitation of T/B ratios is not necessary for visualization and image-guided resection of SLN(s) using fluorescence-based multiplexing strategies. Moreover, it is not possible to correct such data post hoc if the working distance, gain, and exposure time were not recorded at the time of image acquisition. Second, the interpretation of the histopathological panel of assays acquired on nodal tissue specimens was more challenging for those demonstrating predominant melanophages. Specifically, this was demonstrated when quantifying fluorescence intensity values on confocal imaging. Nodal sections with predominant melanophage inclusion, on average, resulted in increased intensity sums in the αMSH-PEG-Cy5.5-C′ dot channel. It was difficult to determine with absolute certainty whether these high summed values reflected specific targeting of tumor cells or were due to the presence of particles in melanophages.

αMSH- and cRGDY-functionalized C′ dots served as real-time imaging biomarkers for interrogating intratumoral heterogeneity and characterizing molecular phenotypes for more than one disease biomarker expressed in our spontaneous melanoma miniswine model with high sensitivity, specificity, and spectral resolution. The high detection sensitivity of these spectrally distinct particle probes (i.e., low nanomolar range; Fig. 3) permitted identification of micrometastatic tumor deposits (i.e., <2 to 3 mm) in several lymph nodes (table S4) by confocal microscopy. In addition, both the PET T/B ratios and the total fluorescence signal obtained on confocal microscopy for these nodes strongly correlated with tumor burden (Fig. 6, L and M) based on the maximum tumor diameter. Similar to

findings in human melanoma subjects (35), tumor burden was also found to be a robust and quantifiable measurement of metastatic nodal disease in this spontaneous melanoma miniswine model. The positive correlation found for these imaging-tissue analyses has led to the use of these procedures in our current SLN mapping clinical trials.

In summary, the implementation of more reliable and accurate image-guided multiplexing tools for real-time visualization of disease, as developed for this study and future ones, is expected to improve surgical staging, facilitate surgical decision-making, reduce surgical risks, and lead to overall better patient outcomes.

MATERIALS AND METHODS
Synthesis and characterization of spectrally distinct ultrasmall fluorescent C′ dots
The synthesis of C′ dots was modified from previously reported protocols (25). More specifically, maleimide-functionalized dye was first dissolved in dimethyl sulfoxide (DMSO) under nitrogen at a concentration of around 0.01 M. The dye/DMSO solution was then mixed with (3-mercaptopropyl)trimethoxysilane (MPTMS) under nitrogen at a dye:MPTMS molar ratio 1:25. The mixture was left under nitrogen overnight to conjugate the dye to the silane group via a thiolene click reaction. Afterward, around 100 μl of the obtained dye-silane precursor was added together with 68 μl of tetramethyl orthosilicate into 10 ml of DI water at pH around 8. The reaction mixture was stirred at room temperature overnight, and 100 μl of PEG-silane (Gelest, molecular weight of around 500) was then added. The reaction mixture was further stirred at room temperature overnight, followed by heat treatment at 80°C overnight. Before particle characterization, the reaction solution was lastly cooled to room temperature, purified by GPC, and sterile filtered. Four types of dyes were used in this study, including Cy5.5, DY782, DY800, and CW800, for the synthesis of C′ dots with different NIR fluorescence characteristics. The synthesis conditions, e.g., reaction time and reagent concentrations, of C′ dots with different types of dyes were slightly varied to optimize both reaction yield and product performance (details not included).

For the synthesis of C′ dots that are further functionalized with targeting peptides, cysteine-functionalized targeting peptide and heterobifunctional PEG (mal-dPEG@12-NHS, Quantum Biodesign) were first separately dissolved in DMSO under nitrogen at a concentration of around 0.021 and 1.2 M, respectively. Mal-dPEG@12-NHS/DMSO solution was then mixed with 3-triethoxysilylpropylamine (APTES, liquid) under nitrogen at a mal-dPEG@12-NHS:APTES molar ratio of 1:0.9. The mixture was left under nitrogen overnight to conjugate the mal-dPEG@12-NHS molecule with a silane group via amine-NHS ester reaction. After that, peptide/DMSO solution was further added into the mixture under nitrogen at peptide:mal-dPEG@12-NHS:APTES molar ratios of 1.1:1:0.9. The mixture was then left under nitrogen overnight to further conjugate the mal-PEG-silane molecule with a targeting peptide via thiol-ene click reaction. Last, around 100 μl of the obtained peptide-PEG-silane precursor was added into the C′ dot synthesis solution right before the addition of PEG-silane to functionalize C′ dots with different types of targeting peptides. Two types of targeting peptides were used in this study, i.e., αMSH (23) and RGDY (22).

Each batch of the obtained NIR C′ dots was characterized by GPC, FCS, ultraviolet-visible (UV-vis) absorption and emission

spectroscopy, and TEM. A BioLogic LP system (Bio-Rad) equipped with a 275-nm UV detector and a self-packed column (Superdex 200 resin, GE Healthcare Life Sciences) were used for GPC purification and characterization. A home-made multichannel FCS setup was used for the characterization of concentration, hydrodynamic size, number of dyes per C′ dot, and number of targeting ligand per C′ dot. A 635-nm solid-state laser was used for the FCS characterization of C′ dots labeled with Cy5.5, while a 780-nm solid-state laser was used for the FCS characterization of C′ dots labeled with either DY782, DY800, or CW800. UV-vis absorbance spectra were measured by a Cary 5000 spectrophotometer (Agilent), and emission spectra were measured by a QuantaMaster spectrofluorometer (Photon Technologies International). TEM images were taken using a T12 Spirit electron microscope (FEI).

In vitro and in vivo detection sensitivity measurements of the Quest Spectrum fluorescence camera system

For the in vitro measurements, αMSH-PEG-Cy5.5-C′ dots and cRGDY-PEG-CW800-C′ dots were used. Three sets of 12 wells each in a 96-well microtiter plate were filled with 250 μl each of serial dilutions in water of αMSH-PEG-Cy5.5-C′ dots, cRGDY-PEG-CW800-C′ dots, or a mixture of αMSH-PEG-Cy5.5-C′ dots and cRGDY-PEG-CW800-C′ dots. The concentration of αMSH-PEG-Cy5.5-C′ dots and cRGDY-PEG-CW800-C′ dots in each set of 12 wells ranged from 1000 to 1 nM; a "blank" well containing only water was included among the 12 wells. Black cardboard with a hole cut out equal in size to that of a well was placed over the microtiter plate, so that only one well was illuminated at a time and that any reflections from the well plate itself were minimized. The camera was positioned 100 mm above the microtiter plate, with exposures of 30 ms used for the 700- and 800-nm sensitive imaging channels and 5 ms for the RGB (white) color channel, and gains of 15 dB used for the 700- and the 800-nm channels and 5 dB for the RGB color channel. The light engine's power output was set to 5.0 and 7.5 mW/cm^2 for the 700- and 800-nm channels, respectively. The net (i.e., background-corrected) mean 700- and 800-nm fluorescence signals in a circular region of interest centered over each well was recorded and used for quantification.

For the in vivo measurements, a nude mouse was subcutaneously injected with mixtures of αMSH-PEG-Cy5.5-C′ dots and cRGDY-PEG-CW800-C′ dots at concentrations of 15, 1.5, and 0.15 μM in the flank at three sites. The subject was illuminated with either 700- or 800-nm excitation light, and the images in the 700- and 800-nm channels were recorded. In addition, "bleed-through" of the Cy5.5 fluorescence signal into the 800-nm channel (or CW800 fluorescence signal into the 700-nm channel) was quantitated. The exposure time was 60 ms, and the camera gain was 15 dB.

^{124}I radiolabeling of cRGDY-PEG-CW800-C′ dots

Radiolabeling of cRGDY-PEG-CW800-C′ dots with ^{124}I was performed using a previously reported IODOGEN method (21, 27). Briefly, 50 μl of 1 M ammonium acetate was added to an iodination tube, followed by 40 μl (15 μM) of cRGDY-PEG-CW800-C′ dots and 2.0 mCi (74 MBq) of ^{124}I sodium iodide. The mixture was gently vortexed for several seconds and maintained at room temperature (22°C) for 10 min. Free radioiodine was removed by passing the mixture through a PD-10 column [phosphate-buffered saline (PBS) as the mobile phase]. The final ^{124}I-cRGDY-PEG-CW800-C′ dots were suspended in PBS for PET imaging study.

Spontaneous melanoma miniswine models for the detection and treatment of nodal metastasis

All animal experiments were performed in accordance with protocols approved by the Institutional Animal Care and Use Committee of the Memorial Sloan Kettering Cancer Center (MSKCC) and followed National Institutes of Health (NIH) guidelines for animal welfare. Metastatic cutaneous melanoma to SLNs has been previously studied by this group (27, 46) and other investigators (11, 42, 47, 48) in the well-characterized Sinclair miniswine spontaneous melanoma model (Sinclair miniature swine, Sinclair Research Center) (24, 49, 50), which accurately recapitulates the human disease. Further, this intermediate-size animal model was ideal for simulating the application of SLN biopsy procedures in humans.

Preoperative PET/CT imaging and surgical planning

Spontaneous melanoma miniswine (4 to 16 kg, Sinclair Research Center) were peritumorally injected with ^{124}I-cRGDY-PEG-CW800-C′ dots (dose range, 19 to 28 MBq) for detecting and localizing metastatic disease using whole-body PET/CT imaging. PET/CT miniswine imaging was performed using a clinical Biograph 64 system (Siemens Medical Solutions USA, Knoxville, TN) at about 60 min following peritumoral injection of 3.6 mCi of ^{124}I-labeled cRGDY-functionalized nanoparticles. CT scanning was performed using an effective milliampere seconds (mAs) of 100, x-ray tube voltage of 120 kilovoltage, pitch of 0.55, rotation time of 1.0 s, and scan time of 17.5 s, yielding 3-mm-thick transverse slices. PET scanning was performed over five bed positions at 2 min per bed position, and images were reconstructed using Siemens' proprietary TrueX iterative algorithm (21 subsets, 10 iterations) in a 512 × 512 matrix and corrected for scatter and attenuation. The sites of the SLNs were then marked (based on the PET/CT scans), shaved, and prepped.

PET imaging analysis

Voxel count rates in the reconstructed PET images were decay corrected and parameterized in terms of SUV = ((mCi found/g of tissue)/(mCi injected/g of body mass)). Three-dimensional region-of-interest analysis of reconstructed images (processed by the Inveon Research Workplace software) yielded tumor and normal organ activity concentrations (i.e., mean, maximum, and SD of the SUV). T/M (or target-to-background) activity concentration ratios were derived by dividing image-derived tumor SUV values by the muscle SUV values.

Image-guided intraoperative fluorescence imaging and surgical treatment of SLNs

Following serial intradermal injections of nonradioactive melanoma-targeted C′ dots (i.e., αMSH-PEG-Cy5.5-C′ dots and cRGDY-PEG-CW800-C′ dots; ~3.5 nmol of each probe in 0.5 ml of DI water), after an average of about 10 min, the animals were then imaged intraoperatively using the Quest Spectrum fluorescence imaging system. Lymphatic channels that ran toward the second echelon nodes were also visualized, followed, and imaged. Real-time multiplexed image-guided SLN dissection was then performed and recorded. Related nodes were then subjected to ex vivo multiplexed imaging before being sent for histopathologic examination. Harvested specimens, as well as nodal basins bilaterally, were evaluated histologically with H&E staining and were additionally stained with specific human melanoma markers according to standard protocols to confirm the presence of melanoma. The primary tumor was also resected and sent to pathological analysis.

Ex vivo tissue processing

Immediately following excision, lymph node tissue samples were sectioned at regular intervals to obtain 2-mm-thick slices. One slice from the center of each sample was freshly frozen in Tissue-Tek O.C.T. Compound (Sakura Finetek, Torrance, CA). All remaining sections, including the primary tumor, were fixed in 10% neutral-buffered formalin, then processed routinely in alcohol and xylene, embedded in paraffin, and sectioned at 5-um thickness for H&E and immunohistochemical staining. H&E-stained sections of lymph nodes and primary tumor were examined to confirm the presence of metastases and primary tumor diagnosis, respectively. Sectioned lymph nodes were also evaluated for the presence of melanophages or any other observable pathologic changes.

Tumor burden measurement

Tumor burden measurements were recorded as the largest diameter of any cluster of pigmented cells within each lymph node, according to an examination of the entire H&E-stained paraffin sections (multiple sections per node, obtained as 2-mm intervals, as described under the "Ex vivo tissue processing" section). For melanin pigment tumor burden assessment, the H&E-stained sections from all 2-mm slices were used: Images of the entire section were acquired with an Olympus BX45 microscope (1.25× objective) equipped with a DP25 camera and cellSens Entry v1.12 software (Olympus America, Waltham, MA) to generate images with a resolution of 5.45 μm per pixel. Using ImageJ (version 1.51; NIH, Bethesda, MD), the color images were first converted to grayscale and subjected to thresholding to detect pigment as positive pixels. After the collection of positive pixel counts across all sections for a given node, a calculation was performed to extrapolate the volume of melanin present within the entire node. For each section, the melanin pigment burden (mm^3) was calculated with the following formula: a number of positive pixels * 2.9703×10^{-5} mm^2 per pixel × 2 mm. The total burden for each node was obtained from the sum of the values calculated for each section from that node, which were obtained at 2-mm intervals. Assessment of all stained sections and tumor burden calculations were performed by an independent, board-certified veterinary pathologist.

Immunohistochemistry

Immunohistochemical staining was performed manually on paraffin-embedded sections. Following bleaching with 10% peroxide, heat-induced epitope retrieval in a citrate buffer (pH 6.0, for MiTF) or EDTA buffer (pH 9.0, for integrin α_v), and routine blocking steps, primary antibodies were applied at the following dilutions: MiTF, 1:500 (Sigma, HPA003259); and integrin α_v, 1:5000 (Abcam, ab179475). Secondary antibodies diluted at 1:500 were then applied (biotinylated anti-rabbit or anti-mouse immunoglobulin G; Vector Laboratories, BA-1000 or BA-2000), followed by an avidin-biotin detection system (Vectastain Elite ABC-HRP Kit, Vector Laboratories) in which the red chromogen was aminoethyl carbazole (AEC). Last, sections were counterstained with hematoxylin and mounted with coverslips using VectaMount AQ Mounting Medium (Vector Laboratories, H-5501).

Western blot

Miniswine lymph nodes deemed to be normal or having high metastatic burden according to pathology reports were thawed from O.C.T. medium and used to perform Western blot analysis. Sections of the thawed nodes were carefully removed using a scalpel and placed in a microcentrifuge tube. The remaining tissue was quickly replaced into new O.C.T. medium and frozen. The tissue sample was then macerated using the Bullet Blender Gold tissue homogenizer (Next Advance) in RIPA lysis and extraction buffer (Thermo Fisher Scientific, 89900). Tissue homogenate was cleared by centrifugation ($13.2g$ for 20 min at 4°C). The protein concentration of the supernatant was quantified using the Bradford Protein Assay (Bio-Rad, 5000001) according to the manufacturer's instructions. Tissue extracts were run on a NuPAGE 4 to 12% Bis-Tris protein gel (Invitrogen, NP0335BOX) and transferred to a polyvinylidene difluoride membrane. Membranes were blocked in 5% milk/0.1% TBS (tris-buffered saline)–Tween 20 (TBST) for 1 hour at room temperature. Following three washes, anti-MiTF antibody (Invitrogen, MS-771-P1) was added at a 1:1000 dilution in 5% milk/0.1% TBST and incubated overnight at 4°C. Membranes were then washed three times before incubation with anti-mouse secondary antibody at 1:2000 (Santa Cruz Biotechnology, sc-2005). Blots were developed using a Pierce ECL Western blotting substrate (Thermo Fisher Scientific, 32106).

High-resolution confocal microscopy

Frozen miniswine lymph node sections were fixed in a 1% paraformaldehyde/PBS solution for 3 min before being incubated with 4′,6-diamidino-2-phenylindole (DAPI) nuclear stain (0.1 mg/ml) for 5 min. Residual DAPI solution was removed, and coverslips were applied using ProLong Gold mounting medium (Thermo Fisher Scientific). Mounted sections were then imaged on a Leica-SP8 point-scanning confocal microscope (Leica Microsystems), operated by the MSKCC Molecular Cytology Core. Individual fluorescent channels were extracted from the image projection, and total fluorescence intensities were calculated using Imaris image analysis software (Bitplane). Fluorescence intensity values were then plotted against histologically assessed tumor burden (maximum diameter) to calculate correlation curves using a linear regression model within Excel (Microsoft). Total fluorescence intensity values of both Cy5.5 and CW800 channels for individual tissue sections were also displayed using Excel.

Whole-section Cy5.5 fluorescence imaging

Miniswine SLNs, provided by the Comparative Pathology Core, were frozen in Tissue-Tek O.C.T. Compound (Sakura Finetek) and sectioned at a thickness of 10 μm on an Avantik Cryostatic Microtome (Avantik Biogroup). Nodes deemed to have "high" and "low" metastatic burden, according to pathology reports, were used to evaluate differences in C′ dot accumulation. Adjacent sections were used for imaging, one undergoing H&E staining and the other Cy5.5 imaging. Images were captured at a fixed exposure on a BX60 fluorescence microscope (Olympus America Inc.) equipped with a motorized stage (Prior Scientific Instruments Ltd.) and a CC12 camera (Olympus America Inc.) at ×10 magnification. Whole-section images were constructed by aligning numerous fields using MicroSuite Biological Suite (version 2.7, Olympus). Bright-field (H&E) and fluorescent (Cy5.5) images were captured using their respective filter sets. Processing of images was performed in Adobe Photoshop (CS6) as previously described (*51*).

Microdose toxicology study of C′ dots in mice

This study assessed the safety of a single subcutaneous injection of αMSH-PEG-Cy5.5-C′ dots or of cRGDY-PEG-CW800-C′ dots in mice, in support of microdose imaging trials. An M21 human melanoma

tumor model was chosen for this study to best represent the clinical context. Healthy male and female 6- to 8-week-old athymic mice were randomly allocated to groups of 15 mice per group per sex (table S5). Mice (groups 5 to 10 and 15 to 20) were inoculated with 5×10^6 M21 (human melanoma) cells in a 50:50 Matrigel:PBS (v/v) solution on the right flank. Once tumors reached 100 to 150 mm^3, animals were assigned to either the control or the treatment group as outlined in table S5. On study day 1, tumor-bearing mice (groups 5 to 10 and 15 to 20) received one single dose of either vehicle or one of the two test articles through a bolus subcutaneous injection. As a control and to account for tumor-related effects, three mice per sex per group (groups 11 to 14 and 21 to 24) were not inoculated with M21 cells and were dosed with either vehicle or one of the two test articles on study day 1. To confirm exposure to test articles, an additional two mice per sex per group were dosed on study day 1 and immediately imaged via IVIS bioluminescence. Upon administration, concentration and stability analysis in the remaining solutions by GPC and FSC were also conducted.

M21 tumor–bearing mice were analyzed for hematology, clinical chemistry, and complete necropsy. Non–tumor-bearing mice controls were processed for hematology, clinical chemistry, and gross necropsy only. Twenty-four hours after dosing, blood was obtained from 10 mice per group per sex (groups 5 to 14), and hematology and clinical chemistry analyses were performed. The same groups of mice were then euthanized and processed for either gross necropsy (non–tumor-bearing mice, groups 11 to 14) or complete histopathology (tumor-bearing mice, groups 5 to 10). The remaining mice were observed for up to 2 weeks before final euthanasia. At the end of the observation period, blood was drawn from mice for hematology and clinical chemistry analyses (groups 15 to 24), and the animals were then euthanized and processed for either gross necropsy (nontumor mice, groups 21 to 24) or complete histopathology (tumor-bearing mice, groups 15 to 20). A comprehensive panel of tissues was evaluated.

IVIS imaging to identify nanoparticle at the tumor site
On study day 1, 15 min after injection, mice in groups 1 to 4 were anesthetized using isoflurane, and whole-body optical fluorescence imaging was acquired to identify nanoparticle fluorescence at the tumor site. Mice were scanned for 0.1 to 1 s using the IVIS spectrum photon-counting device optical imaging system (Xenogen, Alameda, CA) with the blocks and filters for Cy5.5 fluorescence (Ex, 675 nm; Em, 694 nm), CW800 fluorescence (Ex, 778 nm; Em, 794 nm), and background fluorescence (Ex, 465 nm; Em, 600 nm), selected according to the manufacturer's recommendations. Fluorescence background was likewise subtracted according to the manufacturer's instructions. Fluorescence signal was reported as radiant efficiency [(photons/s/cm^2/sr)/mW/cm^2]. This system detected optical signal at the injection site after fluorescent probe administration. Data are summarized in fig. S16.

Mortality
All animals were observed at least daily for mortality from the time of animal receipt through the end of the study.

Body weight
Body weights were recorded for all animals from study days 1 to 14. All mice were observed for clinical symptoms at the time the animals were received and daily from study days 1 to 14.

Hematology
On study day 2 (groups 5 to 14) and study days 11 to 14 (groups 15 to 24), mice were anesthetized with isoflurane, and approximately 100 μl of whole blood was collected from the orbital plexus of each mouse into a labeled tube containing EDTA anticoagulant. Within 2 hours of blood collection, blood samples were analyzed on a HT5 Hematology Analyzer (Heska). The hematology parameters (listed in table S7) recorded are summarized in tables S10 to S29.

Clinical chemistry
On study day 2 (for groups 3 to 6) and study day 14 (groups 7 to 10), mice were anesthetized with isoflurane, and approximately 400 μl of whole blood was collected from the orbital plexus of each mouse into a labeled serum separator tube. After allowing the blood to clot for 30 min at room temperature, the tubes were centrifuged at 4°C for 4 min at 10,000g. Serum was collected and analyzed immediately on a Beckman Coulter AU680 clinical chemistry analyzer. The clinical chemistry parameters (listed in table S8) recorded for each sample are summarized in tables S30 to S49.

Necropsy
On study day 2 (for groups 5 to 14), study day 11 (groups 15 to 20, early euthanasia due to tumor burden), and study day 14 (groups 21 to 24), mice were euthanized via CO$_2$ inhalation. A necropsy was performed on each. Tissues were collected into formalin. No tissues were discarded.

Gross pathology observations
At the time of necropsy, gross examinations of each animal including internal organs were performed by members of the Antitumor Assessment Core Facility, and any macroscopic lesions or other abnormal findings were recorded using standard terminology.

Histopathology
All tissues (except from animals that were found dead) were preserved in formalin. After at least 24 hours in fixative, the tissues listed in table S9 were processed and embedded in paraffin. Paraffin blocks were then sectioned at 4 μm. The resulting unstained slides were then stained with H&E. Slides were then shipped to Comparative Bioscience Inc., and all tissues were examined by a board-certified pathologist. Lesions were recorded using morphologic diagnoses following standardized nomenclature.

Statistical method
Group means and SDs were calculated for body weights, as well as hematology and clinical chemistry parameters. For hematology and clinical chemistries, at each time point, the percent difference between the mean of the test article–treated groups and corresponding vehicle-treated groups was calculated. The statistical significance of these differences was analyzed by unpaired t test and considered statistically significant if $P < 0.05$. Statistical analyses were performed using Ascentos, a Preclinical Laboratory Information Systems Software by PDS Life Sciences.

SUPPLEMENTARY MATERIALS

View/request a protocol for this paper from *Bio-protocol*.

REFERENCES AND NOTES

1. D. G. Coit, J. A. Thompson, A. Algazi, R. Andtbacka, C. K. Bichakjian, W. E. Carson III, G. A. Daniels, D. DiMaio, M. Ernstoff, R. C. Fields, M. D. Fleming, R. Gonzalez, V. Guild, A. C. Halpern, F. S. Hodi Jr., R. W. Joseph, J. R. Lange, M. C. Martini, M. A. Materin, A. J. Olszanski, M. I. Ross, A. K. Salama, J. Skitzki, J. Sosman, S. M. Swetter, K. K. Tanabe, J. F. Torres-Roca, V. Trisal, M. M. Urist, N. McMillian, A. Engh, Melanoma, Version 2.2016, NCCN Clinical Practice Guidelines in Oncology. *J. Natl. Compr. Cancer Netw.* **14**, 450–473 (2016).

2. S. P. Bagaria, M. B. Faries, D. L. Morton, Sentinel node biopsy in melanoma: Technical considerations of the procedure as performed at the john wayne cancer institute. *J. Surg. Oncol.* **101**, 669–676 (2010).

3. M. J. Gerdes, A. Sood, C. Sevinsky, A. D. Pris, M. I. Zavodszky, F. Ginty, Emerging understanding of multiscale tumor heterogeneity. *Front. Oncol.* **4**, 366 (2014).

4. K. Heinzmann, L. M. Carter, J. S. Lewis, E. O. Aboagye, Multiplexed imaging for diagnosis and therapy. *Nat. Biomed. Eng.* **1**, 697–713 (2017).

5. H. Kobayashi, M. R. Longmire, M. Ogawa, P. L. Choyke, S. Kawamoto, Multiplexed imaging in cancer diagnosis: Applications and future advances. *Lancet Oncol.* **11**, 589–595 (2010).

6. R. T. Lucarelli, M. Ogawa, N. Kosaka, B. Turkbey, H. Kobayashi, P. L. Choyke, New approaches to lymphatic imaging. *Lymphat. Res. Biol.* **7**, 205–214 (2009).

7. L. M. A. Crane, G. Themelis, H. J. G. Arts, K. T. Buddingh, A. H. Brouwers, V. Ntziachristos, G. M. van Dam, A. G. J. van der Zee, Intraoperative near-infrared fluorescence imaging

for sentinel lymph node detection in vulvar cancer: First clinical results. *Gynecol. Oncol.* **120**, 291–295 (2011).

8. E. M. Sevick-Muraca, R. Sharma, J. C. Rasmussen, M. V. Marshall, J. A. Wendt, H. Q. Pham, E. Bonefas, J. P. Houston, L. Sampath, K. E. Adams, D. K. Blanchard, R. E. Fisher, S. B. Chiang, R. Elledge, M. E. Mawad, Imaging of lymph flow in breast cancer patients after microdose administration of a near-infrared fluorophore: feasibility study. *Radiology* **246**, 734–741 (2008).

9. X. Montet, K. Montet-Abou, F. Reynolds, R. Weissleder, L. Josephson, Nanoparticle imaging of integrins on tumor cells. *Neoplasia* **8**, 214–222 (2006).

10. H. Kobayashi, M. Ogawa, R. Alford, P. L. Choyke, Y. Urano, New strategies for fluorescent probe design in medical diagnostic imaging. *Chem. Rev.* **110**, 2620–2640 (2010).

11. D. M. Gilmore, O. V. Khullar, S. Gioux, A. Stockdale, J. V. Frangioni, Y. L. Colson, S. E. Russell, Effective Low-dose Escalation of Indocyanine Green for Near-infrared Fluorescent Sentinel Lymph Node Mapping in Melanoma. *Ann. Surg. Oncol.* **20**, 2357–2363 (2013).

12. A. Cousins, S. K. Thompson, A. B. Wedding, B. Thierry, Clinical relevance of novel imaging technologies for sentinel lymph node identification and staging. *Biotechnol. Adv.* **32**, 269–279 (2014).

13. Y. Hama, Y. Koyama, Y. Urano, P. L. Choyke, H. Kobayashi, Two-color lymphatic mapping using Ig-conjugated near infrared optical probes. *J. Invest. Dermatol.* **127**, 2351–2356 (2007).

14. Y. Koyama, T. Barrett, Y. Hama, G. Ravizzini, P. L. Choyke, H. Kobayashi, In vivo molecular imaging to diagnose and subtype tumors through receptor-targeted optically labeled monoclonal antibodies. *Neoplasia* **9**, 1021–1029 (2007).

15. C.-W. Yen, H. de Puig, J. O. Tam, J. Gomez-Marquez, I. Bosch, K. Hamad-Schifferli, L. Gehrke, Multicolored silver nanoparticles for multiplexed disease diagnostics: Distinguishing dengue, yellow fever, and Ebola viruses. *Lab Chip* **15**, 1638–1641 (2015).

16. R. Deng, F. Qin, R. Chen, W. Huang, M. Hong, X. Liu, Temporal full-colour tuning through non-steady-state upconversion. *Nat. Nanotechnol.* **10**, 237–242 (2015).

17. C.-W. Peng, X.-L. Liu, C. Chen, X. Liu, X.-Q. Yang, D.-W. Pang, X.-B. Zhu, Y. Li, Patterns of cancer invasion revealed by QDs-based quantitative multiplexed imaging of tumor microenvironment. *Biomaterials* **32**, 2907–2917 (2011).

18. C. L. Zavaleta, B. R. Smith, I. Walton, W. Doering, G. Davis, B. Shojaei, M. J. Natan, S. S. Gambhir, Multiplexed imaging of surface enhanced Raman scattering nanotags in living mice using noninvasive Raman spectroscopy. *Proc. Natl. Acad. Sci. U.S.A.* **106**, 13511–13516 (2009).

19. Y. Wang, S. Kang, A. Khan, G. Ruttner, S. Y. Leigh, S. Murray, S. Abeytunge, G. Peterson, M. Rajadhyaksha, S. Dintzis, S. Javid, J. T. Liu, Quantitative molecular phenotyping with topically applied SERS nanoparticles for intraoperative guidance of breast cancer lumpectomy. *Sci. Rep.* **6**, 21242 (2016).

20. L. Wang, M. B. O'Donoghue, W. Tan, Nanoparticles for multiplex diagnostics and imaging. *Nanomedicine (London)* **1**, 413–426 (2006).

21. E. Phillips, O. Penate-Medina, P. B. Zanzonico, R. D. Carvajal, P. Mohan, Y. Ye, J. Humm, M. Gonen, H. Kalaigian, H. Schoder, H. W. Strauss, S. M. Larson, U. Wiesner, M. S. Bradbury, Clinical translation of an ultrasmall inorganic optical-PET imaging nanoparticle probe. *Sci. Transl. Med.* **6**, 260ra149 (2014).

22. F. Chen, K. Ma, L. Zhang, B. Madajewski, P. Zanzonico, S. Sequeira, M. Gonen, U. Wiesner, M. S. Bradbury, Target-or-clear zirconium-89 labeled silica nanoparticles for enhanced cancer-directed uptake in melanoma: A comparison of radiolabeling strategies. *Chem. Mater.* **29**, 8269–8281 (2017).

23. F. Chen, X. Zhang, K. Ma, B. Madajewski, M. Benezra, L. Zhang, E. Phillips, M. Z. Turker, F. Gallazzi, O. Penate-Medina, M. Overholtzer, M. Pauliah, M. Gonen, P. Zanzonico, U. Wiesner, M. S. Bradbury, T. P. Quinn, Melanocortin-1 Receptor-Targeting Ultrasmall Silica Nanoparticles for Dual-Modality Human Melanoma Imaging. *ACS Appl. Mater. Interfaces* **10**, 4379–4393 (2018).

24. M. L. Misfeldt, D. R. Grimm, Sinclair miniature swine: an animal model of human melanoma. *Vet. Immunol. Immunopathol.* **43**, 167–175 (1994).

25. K. Ma, C. Mendoza, M. Hanson, U. Werner-Zwanziger, J. Zwanziger, U. Wiesner, Control of Ultrasmall Sub-10 nm Ligand-Functionalized Fluorescent Core–Shell Silica Nanoparticle Growth in Water. *Chem. Mater.* **27**, 4119–4133 (2015).

26. K. Ma, D. Zhang, Y. Cong, U. Wiesner, Elucidating the mechanism of silica nanoparticle PEGylation processes using fluorescence correlation spectroscopies. *Chem. Mater.* **28**, 1537–1545 (2016).

27. M. Benezra, O. Penate-Medina, P. B. Zanzonico, D. Schaer, H. Ow, A. Burns, E. DeStanchina, V. Longo, E. Herz, S. Iyer, J. Wolchok, S. M. Larson, U. Wiesner, M. S. Bradbury, Multimodal silica nanoparticles are effective cancer-targeted probes in a model of human melanoma. *J. Clin. Invest.* **121**, 2768–2780 (2011).

28. D. R. Larson, H. Ow, H. D. Vishwasrao, A. A. Heikal, U. Wiesner, W. W. Webb, Silica Nanoparticle Architecture Determines Radiative Properties of Encapsulated Fluorophores. *Chem. Mater.* **20**, 2677–2684 (2008).

29. K. P. Barteau, K. Ma, F. F. E. Kohle, T. C. Gardinier, P. A. Beaucage, R. E. Gillilan, U. Wiesner, Quantitative measure of the size dispersity in ultrasmall fluorescent organic–inorganic hybrid core–shell silica nanoparticles by small-angle X-ray scattering. *Chem. Mater.* **31**, 643–657 (2019).

30. E. Herz, T. Marchincin, L. Connelly, D. Bonner, A. Burns, S. Switalski, U. Wiesner, Relative quantum yield measurements of coumarin encapsulated in core-shell silica nanoparticles. *J. Fluoresc.* **20**, 67–72 (2010).

31. E. Herz, H. Ow, D. Bonner, A. Burns, U. Wiesner, Dye structure–optical property correlations in near-infrared fluorescent core-shell silica nanoparticles. *J. Mater. Chem.* **19**, 6341–6347 (2009).

32. E. Herz, A. Burns, D. Bonner, U. Wiesner, Large stokes-shift fluorescent silica nanoparticles with enhanced emission over free dye for single excitation multiplexing. *Macromol. Rapid Commun.* **30**, 1907–1910 (2009).

33. B. Cohen, C. Martin, S. K. Iyer, U. Wiesner, A. Douhal, Single Dye Molecule Behavior in Fluorescent Core–Shell Silica Nanoparticles. *Chem. Mater.* **24**, 361–372 (2012).

34. E. R. Price, M. A. Horstmann, A. G. Wells, K. N. Weilbaecher, C. M. Takemoto, M. W. Landis, D. E. Fisher, alpha-Melanocyte-stimulating hormone signaling regulates expression of *microphthalmia*, a gene deficient in Waardenburg syndrome. *J. Biol. Chem.* **273**, 33042–33047 (1998).

35. M. E. Egger, M. R. Bower, I. A. Czyszczon, H. Farghaly, R. D. Noyes, D. S. Reintgen, R. C. Martin II, C. R. Scoggins, A. J. Stromberg, K. M. McMasters, Comparison of sentinel lymph node micrometastatic tumor burden measurements in melanoma. *J. Am. Coll. Surg.* **218**, 519–528 (2014).

36. J. M. Ranieri, J. D. Wagner, R. Azuaje, D. Davidson, S. Wenck, J. Fyffe, J. J. Coleman III, Prognostic importance of lymph node tumor burden in melanoma patients staged by sentinel node biopsy. *Ann. Surg. Oncol.* **9**, 975–981 (2002).

37. G. W. Carlson, D. R. Murray, V. Thourani, A. Hestley, C. Cohen, The definition of the sentinel lymph node in melanoma based on radioactive counts. *Ann. Surg. Oncol.* **9**, 929–933 (2002).

38. R. King, P. B. Googe, K. N. Weilbaecher, M. C. Mihm Jr., D. E. Fisher, Microphthalmia transcription factor expression in cutaneous benign, malignant melanocytic, and nonmelanocytic tumors. *Am. J. Surg. Pathol.* **25**, 51–57 (2001).

39. K. J. Busam, K. Iversen, K. C. Coplan, A. A. Jungbluth, Analysis of microphthalmia transcription factor expression in normal tissues and tumors, and comparison of its expression with S-100 protein, gp100, and tyrosinase in desmoplastic malignant melanoma. *Am. J. Surg. Pathol.* **25**, 197–204 (2001).

40. R. W. Oxenhandler, J. Berkelhammer, G. D. Smith, R. R. Hook Jr., Growth and regression of cutaneous melanomas in Sinclair miniature swine. *Am. J. Pathol.* **109**, 259–269 (1982).

41. J. Wallace, Humane endpoints and cancer research. *ILAR J.* **41**, 87–93 (2000).

42. E. Tanaka, H. S. Choi, H. Fujii, M. G. Bawendi, J. V. Frangioni, Image-guided oncologic surgery using invisible light: Completed pre-clinical development for sentinel lymph node mapping. *Ann. Surg. Oncol.* **13**, 1671–1681 (2006).

43. V. Almendro, A. Marusyk, K. Polyak, Cellular heterogeneity and molecular evolution in cancer. *Annu. Rev. Pathol.* **8**, 277–302 (2013).

44. G. Ravizzini, B. Turkbey, T. Barrett, H. Kobayashi, P. L. Choyke, Nanoparticles in sentinel lymph node mapping. *Wiley Interdiscip. Rev. Nanomed. Nanobiotechnol.* **1**, 610–623 (2009).

45. H. S. Choi, J. V. Frangioni, Nanoparticles for biomedical imaging: Fundamentals of clinical translation. *Mol. Imaging* **9**, 291–310 (2010).

46. M. S. Bradbury, E. Phillips, P. H. Montero, S. M. Cheal, H. Stambuk, J. C. Durack, C. T. Sofocleous, R. J. Meester, U. Wiesner, S. Patel, Clinically-translated silica nanoparticles as dual-modality cancer-targeted probes for image-guided surgery and interventions. *Integr. Biol.* **5**, 74–86 (2013).

47. H. Uhara, N. Yamazaki, H. Takata, Y. Inoue, A. Sakakibara, Y. Nakamura, K. Suehiro, A. Yamamoto, R. Kamo, K. Mochida, H. Takenaka, T. Yamashita, T. Takenouchi, S. Yoshikawa, A. Takahashi, J. Uehara, M. Kawai, H. Iwata, T. Kadono, Y. Kai, S. Watanabe, S. Murata, T. Ikeda, H. Fukamizu, T. Tanaka, N. Hatta, T. Saida, Applicability of radiocolloids, blue dyes and fluorescent indocyanine green to sentinel node biopsy in melanoma. *J. Dermatol.* **39**, 336–338 (2012).

48. Y. Kono, R. Tanaka, A. Tsutsumida, N. Yamazaki, H. Kitamura, T. Aso, H. Kurihara, M. Fukushi, Sentinel lymph node mapping of melanoma using technetium-99m phytate by a hybrid single-photon emission computed tomography/computed tomography. *J. Dermatol.* **41**, 655–656 (2014).

49. R. W. Oxenhandler, E. H. Adelstein, J. P. Haigh, R. R. Hook Jr., W. H. Clark Jr., Malignant melanoma in the Sinclair miniature swine: An autopsy study of 60 cases. *Am. J. Pathol.* **96**, 707–720 (1979).

50. L. E. Millikan, J. L. Boylon, R. R. Hook, P. J. Manning, Melanoma in Sinclair swine: A new animal model. *J. Invest. Dermatol.* **62**, 20–30 (1974).

51. H. Zhang, P. Desai, Y. Koike, J. Houghton, S. Carlin, N. Tandon, K. Touijer, W. A. Weber, Dual-modality imaging of prostate cancer with a fluorescent and radiogallium-labeled gastrin-releasing peptide receptor antagonist. *J. Nucl. Med.* **58**, 29–35 (2017).

Citation: F. Chen, B. Madajewski, K. Ma, D. Karassawa Zanoni, H. Stambuk, M. Z. Turker, S. Monette, L. Zhang, B. Yoo, P. Chen, R. J. C. Meester, S. de Jonge, P. Montero, E. Phillips, T. P. Quinn, M. Gönen, S. Sequeira, E. de Stanchina, P. Zanzonico, U. Wiesner, S. G. Patel, M. S. Bradbury, Molecular phenotyping and image-guided surgical treatment of melanoma using spectrally distinct ultrasmall core-shell silica nanoparticles. *Sci. Adv.* **5**, eaax5208 (2019).